

THAT LOOKS ABOUT RIGHT!



**UNIVERSITY OF CALIFORNIA
SAN DIEGO**

2021-2022

**AIAA DESIGN, BUILD, FLY
DESIGN REPORT**

TABLE OF CONTENTS

§ 1	Executive summary	3	page
§ 2	Management Summary	4	page
	2.1 • Team organization and personnel	4	
	2.2 • Project Timeline	5	
	2.3 • Impact of COVID-19 and other external factors	6	
§ 3	Conceptual design	7	page
	3.1 • Competition overview and scoring	7	
	3.2 • Sensitivity analysis	9	
	3.3 • Translation into design requirements	10	
	3.4 • Configuration selection	11	
	3.5 • Final conceptual design	19	
§ 4	Preliminary design	20	page
	4.1 • Overall design methodology	20	
	4.2 • Propulsion analysis	21	
	4.3 • Fuselage sizing	24	
	4.4 • Wing sizing	24	
	4.5 • Aerodynamic analysis	25	
	4.6 • Stability and control analysis	29	
	4.7 • Mission model	31	
§ 5	Detail design	33	page
	5.1 • Final design parameters	33	
	5.2 • Structural characteristics	34	
	5.3 • System and subsystem architecture	35	
	5.4 • Weight and balance	41	
	5.5 • Expected performance	41	
	5.6 • Drawing package	43	
§ 6	Manufacturing plan	44	page
	6.1 • Investigation of manufacturing processes	44	
	6.2 • Assembly method selection	44	
	6.3 • Manufacturing timeline	46	
§ 7	Testing plan	47	page
	7.1 • Testing schedule	47	
	7.2 • Ground testing	47	
	7.3 • Flight testing	49	
§ 8	Performance results	51	page
	8.1 • Aircraft and subsystem performance	51	
	8.2 • Flight performance	52	
	8.3 • Future work and concluding remarks	52	
§ 9	Bibliography	53	page

1. Executive Summary

This report, presented by the Design/Build/Fly team at the University of California, San Diego (UCSD DBF), details the team's planned approach for the design, analysis, manufacturing, and testing of an unmanned electric radio-controlled model aircraft for participation in the American Institute of Aeronautics and Astronautics' Design/Build/Fly 2021-2022 competition.

This year's team was composed of members who had never attended an in-person competition. Additionally, the team faced various administrative obstacles that limited our access to facilities, materials, and in-person collaboration. In the face of these challenges, however, the team sought to build upon the knowledge and skills of previous years' teams in order to design an aircraft that would meet or exceed the competition performance of earlier years. The team's main objective is to fly an aircraft at this year's competition that successfully completes all three missions specified in the 2022 DBF Competition Rules. Using the final score of the 2019 team (the last team to attend an in-person competition) as a benchmark, this year's team aims to earn a score within the top $\frac{1}{3}$ of all competitors. Guided by the DBF 2022 mission requirements (§ 3.1), the team worked to design an aircraft capable of stable and rapid take-off, flight, and landing in both loaded and unloaded fuselage configurations. Critically, the aircraft also required the ability to securely store and deploy sensitive cargo in the form of vaccine vial boxes.

The UCSD DBF team, consisting of 27 members in 6 subteams (§ 2.1), first developed a sensitivity analysis in order to identify the crucial scoring parameters and guide their design process (§ 3.2). During the conceptual design phase, the team explored a range of subsystem configurations (§ 3.4), including wing and tail type, propulsion system, and cargo storage, with intense scrutiny being placed on the deployment method for Mission 3. The chosen conceptual design was a T-tail dual-motor monoplane with a tapered high-wing, square fuselage, tricycle landing gear, and scissor-lift deployment mechanism (§ 3.5). The design was chosen for its carrying capacity, stability in flight, and manufacturability.

During the preliminary design stage (§ 4), the subteams performed aerodynamic and propulsion trade studies and analyses in order to build upon, optimize, and modify the decisions made in the previous stage. During the detail design phase (§ 5), the aircraft's structural makeup, subsystem organization, and balancing were finalized in order to prepare for manufacturing (§ 6) and testing (§ 7). **Table 1.i** summarizes the final capabilities of the completed aircraft. The team is expected to score approximately **6.1** points and place within the top **5%** of the competition.

	<i>Lap Time</i>	<i>Payload Weight</i>	<i>Payload Type</i>
Mission 1	35.7 s	0 lb	-
Mission 2	31.8 s	4.0 lb	90 syringes
Mission 3	33.7 s (including climb and descent)	4.5 lb	9 vaccine vial boxes

Table 1.i • Final capabilities of the UCSD DBF aircraft.

Additional sections of this report discuss UCSD DBF's project schedule (§ 2.2) and, crucially, the impact of the ongoing COVID-19 pandemic on the team's operations (§ 2.3).

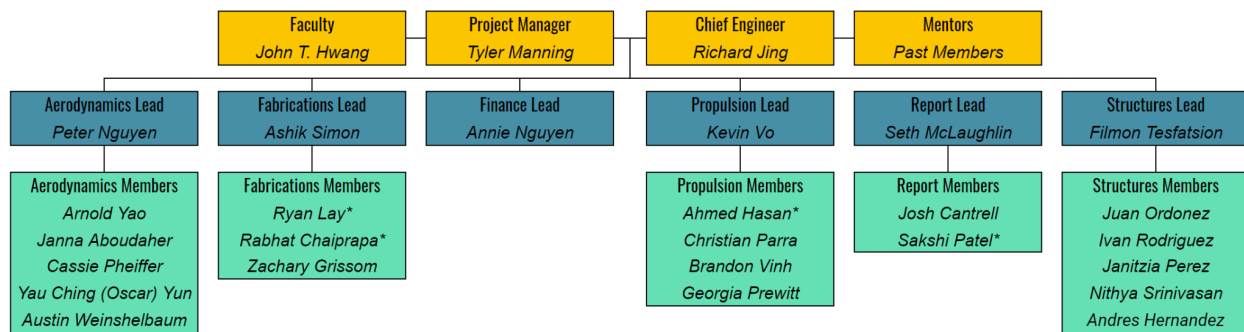
2. Management Summary

The following section details UCSD DBF's organization and outlines the team's project timeline. It also discusses in detail the impact that the ongoing COVID-19 pandemic has had on their schedule.

2.1 Team Organization and Personnel

UCSD DBF is organized in a hierarchical structure. The team is led by a project manager and a chief engineer. The project manager is responsible for organization and logistics, including communication with the faculty advisor and other UCSD engineering staff, planning and organizing meetings, and ensuring that the team maintains its project schedule. The chief engineer supervises the overall design process and leads the systems-level engineering. These two leading members have the final say in all design decisions and supervise six sub-teams. Each sub-team "lead" directs their respective sub-team, trains new members, and reports to the other lead members at weekly meetings. Non-lead members may be a part of one or multiple sub-teams, and their responsibilities vary between sub-teams. Members of each subteam are sufficiently trained such that they can succeed outgoing team members in future years. A visual of the UCSD DBF team structure can be found in **Figure 2.a**.

Sub-teams meet weekly to discuss design considerations, delegate tasks, and train new members. The outcome of each sub-team meeting is discussed at weekly lead meetings between the leads, the project manager, and the chief engineer. Discussion at these lead meetings is the primary mechanism in the design decision-making process. The lead members also meet with the faculty advisor on a semi-regular basis to ask design-related questions and review decisions.



* contributed to more than one subteam

Figure 2.a • UCSD DBF Team structure

The subteam disciplines that make up the UCSD DBF include: Aerodynamics, Fabrications, Finance, Propulsion, Report, and Structures. Each of these subteams, as shown in **Table 2.i**, has unique responsibilities and tasks that are fulfilled in order to create the competition aircraft.

Subteam	Function
Aerodynamics	Designs control surfaces, selects airfoils, and sizes wing and tail to minimize drag.
Fabrication	Builds and assembles aircraft components; defines manufacturing limitations.
Finance	Handles purchases and expenses, networks with industry, and secures funds.
Propulsion	Conducts thrust stand tests; sizes motor, propeller, and battery to optimize thrust.
Report	Communicates competition rules; writes and edits proposals and reports.
Structures	Conducts structural analyses and integrity tests; designs aircraft components.

Table 2.i • The list of subteams and their respective responsibilities.

2.2 Project Timeline

UCSD DBF prepared a timeline for the 2021-2022 competition season. Shown in **Figure 2.b** is the project timeline as prepared for in the design proposal at the end of October 2021, which includes four deadlines for the team's main objectives, marked in red. In the figure, the green marked spaces describe the planned time for each part of the design, fabrication, and testing process. The fabrication process was considered complete when the components were integrated into the aircraft. The spaces marked in yellow show what times the team actually worked on the aircraft.

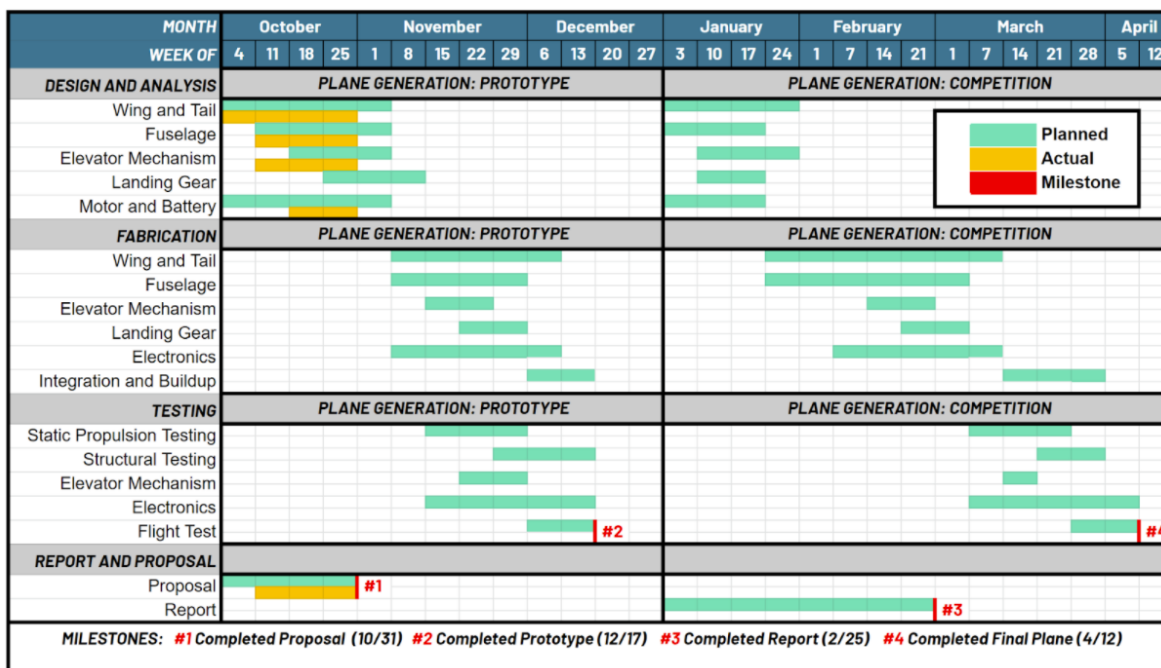


Figure 2.b • UCSD DBF project timeline as of October 2021.

Figure 2.c shows the updated timeline; note that one significant difference with the new timeline is the combination of the plane generations (prototype and competition) to one unified timeline. Significant delays over the course of the academic year were primarily caused by the temporary relocation of DBF materials by the university and the shutdown of group meetings during the COVID-19 Omicron outbreak.

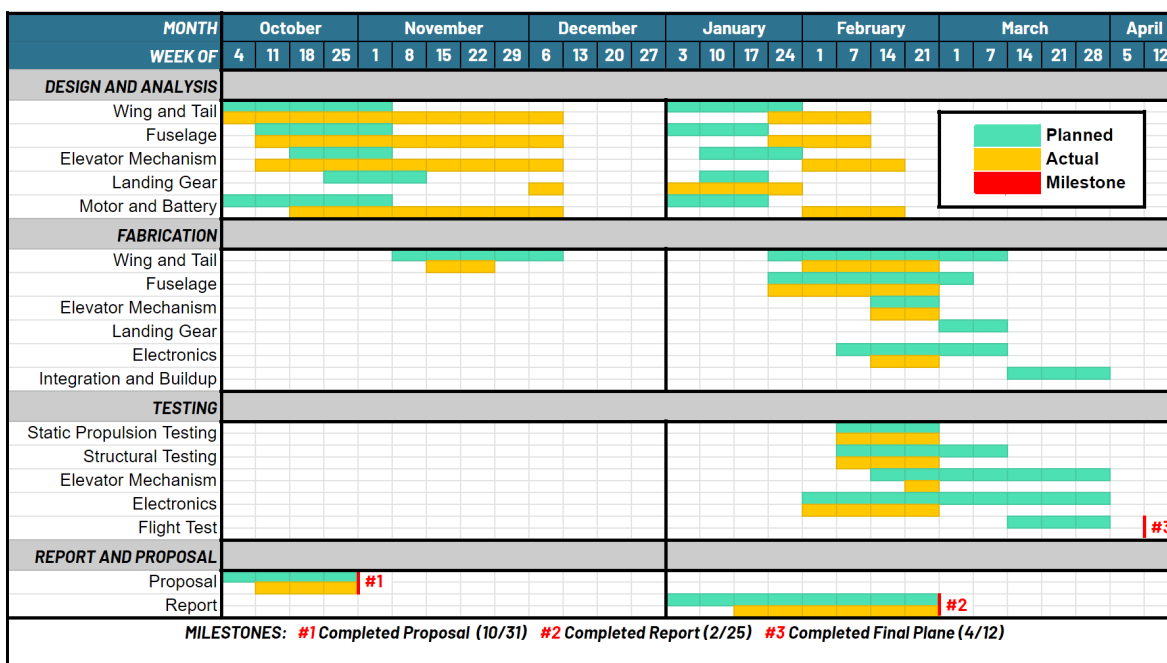


Figure 2.c • Current UCSD DBF project timeline.

2.3 Impact of COVID-19 and other external factors

In early November 2021, UCSD DBF encountered an issue regarding its build room. The room had been evacuated of DBF's supplies over the summer so that the space could undergo renovations. The student organization that supplies the team's workspace, Triton Engineering Student Council, notified UCSD DBF that the renovations for the room would not be completed until at least January. The team immediately searched for an alternative room to work in and found help from our faculty advisor. Dr. Hwang helped acquire a room for UCSD DBF to use, though it would not be ready until December. The fabrication subteam attempted some rudimentary tasks in whatever space could be found until then, though only some marginal progress on the wing and tail were made, further delaying the development of the aircraft.

In December 2021, all UCSD students received notification that one, all winter quarter classes would be mandated to shift to remote instruction, two, all on-campus meetings would be prohibited, and three, UCSD would be providing incentives to limit and stagger the return of students to campus. These changes were in effect for the first four weeks of 2022, barring DBF from the fabrication progress. Separated from each other, our fabrication materials, and our build room, UCSD DBF completed as much work that would be able to be done remotely as possible, waiting for the day that we could return to campus again. Short of a team member building the airplane themselves and bringing it back to campus in February (though this was attempted, it proved too challenging in several aspects for our fabrication lead), the team would have no other options for the time.

As a result of these significant impacts on our initial timeline, the team decided to cut the prototype generation out entirely. Instead, we built for the competition immediately after returning to campus, getting as much work done before the report as possible. This change is reflected in the new timeline, though the old goal milestones still remain as a helpful guide for current progress.

3. Conceptual Design

This section summarizes the first stage of the aircraft's design process. The team identified mission requirements and design restraints, performed a sensitivity analysis, then developed a series of design and subsystem requirements to motivate the development of an initial aircraft design.

3.1 Competition overview and scoring

The team's first goal of the conceptual design process was to gain a full understanding of the year's rules and missions. The following subsection provides a summary of the most important points.

The 2022 AIAA DBF competition consists of one ground mission and three flight missions. Each mission, defined by unique scoring parameters, contributes to the team's final score. The report score serves as a multiplier upon the summed mission scores to give the final score (**Equation 3.1**).

$$S_{FINAL} = S_{REPORT} \times (S_{GROUND} + S_{M1} + S_{M2} + S_{M3}) \quad \text{Equation 3.1}$$

Assuming that the team and aircraft are able to successfully complete each of the four missions, they will earn a summed mission score between 3 and 8 points, with the report score adjusting it accordingly. The remainder of this report is presented under the assumption that all four missions are successfully executed.

3.1.1 • Ground Mission

During the ground mission, the team's designated assembly crew member will load and unload the full Mission 2 payload, and then load the full Mission 3 payload. The full Mission 3 payload will then be deployed using the remote deployment mechanism. The mission will test the ease and efficiency with which the cargo can be loaded and unloaded, as well as ensure that the deployment mechanism is fully operational. The team's score will be determined by normalizing the fastest completion time of the competition with the team's own completion time (**Equation 3.2**).

$$S_{GROUND} = \frac{T_{FASTEST}}{T_{UCSD}} \quad \text{Equation 3.2}$$

3.1.2 • Flight Overview

The aircraft will follow an identical path during each flight mission. The path consists of two 1,000-foot straights connected at either end by 180° turns and a single 360° turn in the middle of the downward straight. The aircraft is allowed a 25-foot takeoff length for each flight mission. **Figure 3.a** shows the flight path broken into flight components.

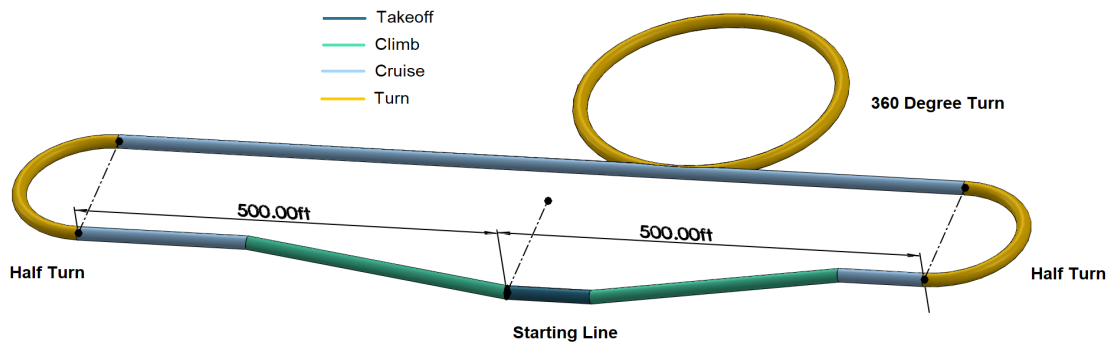


Figure 3.a • The flight path for the 2022 DBF fly-off. Both takeoffs and landings are shown, but do not necessarily occur every lap.

3.1.3 • Mission 1

The first flight mission serves as proof of the aircraft's baseline flight capabilities. In order to secure the single point for a successful mission (**Equation 3.3**), the aircraft must complete 3 full laps in under 5 minutes. This must be followed by a successful landing which is not subject to the 5-minute time restriction. No payload is carried.

$$S_{M1} = 1 \quad \text{Equation 3.3}$$

3.1.4 • Mission 2

The second flight mission demonstrates the aircraft's ability to fly with a maximized payload in the form of disposable plastic syringes. After the syringes are loaded prior to flight, the aircraft must fly 3 full laps in under 5 minutes, identical to Mission 1. The team's Mission 2 score is a function of the number of syringes loaded and the time taken to complete the mission, normalized by the top Mission 2 score of the competition (**Equation 3.4**).

$$S_{M2} = 1 + \frac{(s/t)_{UCSD}}{(s/t)_{MAX}} \quad \text{Equation 3.4}$$

3.1.5 • Mission 3

The third flight mission simulates the transport and delivery of sensitive vaccine vial boxes. Prior to the flight, the aircraft is manually loaded with these simulant boxes, each of which is equipped with a 25G shock sensor at each of its axes. The aircraft must then take off, fly a single lap, land, taxi to a designated dropoff zone, remotely deploy a box, then take off again. This process is repeated until the mission's 10-minute time limit is reached, or until all of the aircraft's boxes have been deployed. The score is determined by the number of boxes deployed (**Equation 3.5**); boxes whose shock sensors have tripped do not count towards the final score.

$$S_{M3} = 2 + \frac{D_{UCSD}}{D_{MAX}} \quad \text{Equation 3.5}$$

Critically, the maximum number of boxes that can be flown in Mission 3, as stated in the rules, is one-tenth of the number of syringes flown in Mission 2, rounded down to the nearest whole number.

3.1.6 • Design Constraints

The design constraints that were identified by the team through the mission requirements and rules document are summarized in **Table 3.i**.

Category	Constraint
General	<ul style="list-style-type: none"> • Maximum allowable wingspan is 8 feet. • Takeoff field length is 25 feet for all missions.
Syringe (Mission 2) Payload	<ul style="list-style-type: none"> • Number of syringes carried must be ten times the number of boxes carried.
Vaccine Vial Box (Mission 3) Payload	<ul style="list-style-type: none"> • 25G sensors on boxes must not be tripped. • Number of boxes carried must be one-tenth the number of syringes carried.
Power Supply	<ul style="list-style-type: none"> • All power for takeoff and flight must be sourced from the aircraft's propulsion system. • Batteries must be either LiPo or NiCad/NIMH. • All batteries used must be identical. • Total stored propulsion energy may not exceed 100 watt-hours.

Table 3.i • Design constraints according to the DBF 2022 Rules.

3.2 Sensitivity Analysis

A scoring sensitivity analysis was developed early in the design process in order to quantify which of the parameters outlined in the scoring equations had the greatest impact on the overall score. The model, designed in MATLAB, considers five variables: report score, time taken to complete Mission 2, the number of syringes carried in Mission 2, the number of boxes carried in Mission 3, and the Ground Mission score. By adjusting the value of one parameter while keeping others constant, the team identified their individual impacts on the total score.

The team utilized data from previous competitions in order to generate best-guess baselines for the model (**Table 3.ii**); namely, the team used fuselage measurement data from previous cargo-based competitions in order to gain an upper estimate on syringe carrying capacity. In order to gain more accurate mission score estimates, the model also assumed that the aircraft's performance would be successful enough to score two standard deviations above the average competition score.

Variable	Initial Guess
Report Score	0.8
Time in Mission 2	120 seconds
Syringe Count	70
Container Count	7
Ground Score	≈33% of top GM score

Table 3.ii • Initial best-guess scoring estimates.

Because it was not yet possible to make meaningful estimations of Ground Mission time, the Ground Mission scores were instead modeled as percentages of the best competition score. **Figure 3.b** shows the results of the analysis. The syringe and box lines are shown as step functions since they can only exist as integer values. The larger jumps on the syringe line indicate a point where the syringe count passes a multiple of 10, which also results in an increase of 1 to the maximum number of boxes that can be carried; these combined effects lead to the estimated score changing more dramatically at these points. The sensitivity analysis showed that, after the report score, the syringe count would have the greatest influence on the final score.

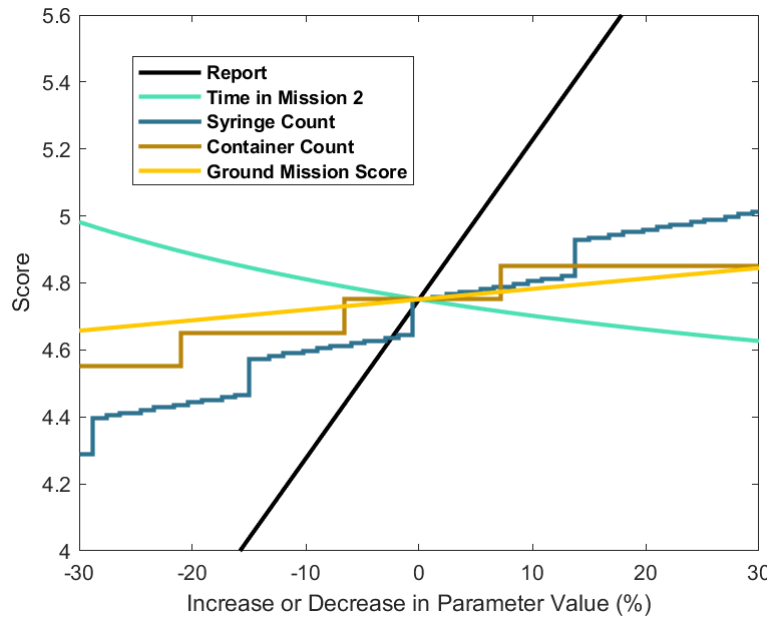


Figure 3.b • Impact of each scoring parameter on the overall competition score.

3.3 Translation into design requirements

With the sensitivity analysis complete, the team was better able to identify design choices that would allow the aircraft to perform well in the competition.

3.3.1 • Fuselage

The volumetric carrying capacity of the fuselage was identified as a major design concern in the early stages of the design process.

3.3.2 • Wing and tail

Mid-flight stability across various weight distributions was determined to be a crucial design parameter due to the presence of the shock sensors and changing payload distribution in Mission 3. It was also necessary to identify an optimal airfoil, wing sizing, and tail sizing combination at the expected mission weight and cruise velocity in order to maximize efficiency.

3.3.3 • Deployment mechanism

The Mission 3 deployment mechanism posed a unique design challenge to the team. The main design consideration of the mechanism was its ability to deploy the vaccine vial boxes without triggering any of the three shock sensors. The mechanism must also have minimal volume so as to have the least impact on the aircraft's carrying capacity.

3.3.4 • Propulsion system

A competitive speed, as always, was deemed necessary in order to minimize time in Mission 2 and maximize the number of vaccine vial box deliveries in Mission 3. Endurance was also identified as an important consideration for Mission 3 due to the increased power requirements of multiple takeoffs and landings.

3.3.5 • Other design considerations

- A proper landing gear system, robust enough to survive multiple landings, was identified as an important aircraft component.
- Since the aircraft must be able to quickly taxi to its deployment zone and to the takeoff line in Mission 3, it was noted that the propulsion and landing gear subsystems must provide for a reasonable level of control when taxiing the aircraft.
- Given that the combined payloads for Missions 2 and 3 were expected to consist of several dozen individual components, the team agreed that an easily-accessible cargo space would be necessary to ensure speed during the loading and unloading portion of the Ground Mission.

3.4 Configuration Selection

Table 3.iii below provides a summary of the most important design considerations identified in the previous subsection. The requirements are ranked in order of importance from top to bottom and provided the basis by which designs were considered.

<i>Consideration</i>	<i>Weight</i>
Carrying Capacity	5
Control and Stability	4
Aerodynamics	3
Manufacturability	3
Structural Strength	3
Deployment Capabilities	2

Table 3.iii • UCSD DBF's design considerations, ranked in order of their importance to achieving the team's objective.

Carrying capacity was clearly a crucial design parameter due to the nature of Missions 2 and 3. Given the low weights of both payloads, the design was restricted mainly by volume rather than mass.

Control and stability were given high priority due to the overarching necessity for the aircraft to be capable of safe, reliable flight. The inevitable variation of weight distribution within the aircraft throughout Mission 3 as boxes were deployed was expected to be a major challenge in satisfying this design requirement. As a secondary consideration, the team recognized that responsive ground controls would lead to quicker, more efficient taxiing and deployment of the boxes.

Aerodynamics, instrumental to the aircraft's velocity, efficiency, and overall mission completion time, was deemed an important factor due to its influence on the Mission 2 and Mission 3 scores.

Manufacturability played a considerable role in the team's decisions throughout the decision process, more so in the past two years than in years prior. The COVID-19 pandemic and the related policies levied on UCSD DBF by the UC San Diego administration made it difficult to access desired manufacturing equipment in a timely and reliable manner.

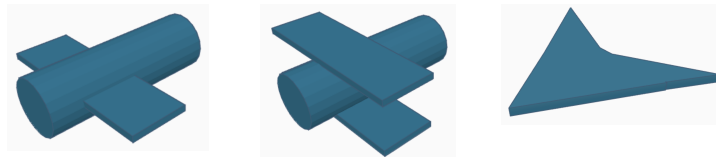
Structural strength must be incorporated in order to ensure a safe flight. It is a concern for all subsystems of the aircraft, but increased scrutiny was applied to the landing gear, due to the repeated landings it would undergo, and cargo storage and deployment mechanism, due to the sensitivity of the 25G sensors that they would be directly interacting with.

Deployment capabilities incorporate the speed, ease, and effectiveness with which the Missions 2 and 3 payloads can be loaded and deployed. While important, these topics were given a lower priority. This is mainly due to the relatively low weight of the Ground Mission score, the only mission for which rapid loading of payload is a factor, on the final score. Deployment speed, additionally, was considered secondary to ensuring that the deployment method is gentle enough to avoid tripping the 25G sensors.

Ultimately, the team decided to design an aircraft inspired by a modern cargo plane. The subsequent subsections detail the decision process and motivation behind 10 design elements that collectively determine the aircraft's ability to carry sufficient payload while maintaining stable flight and a competitive speed.

Figures of merit allowed the team to evaluate potential configurations with the overarching design consideration. Each design element is judged with respect to the 6 design considerations outlined in the above chart and assigned a rating between 1 and 5. This rating is multiplied by the consideration's "weight" value, a measure of its importance to the aircraft's success. Through this process, the team was able to quantitatively consider all configurations in reference to each other and to the design requirements in order to perform necessary design compromises. Certain considerations do not have ratings because they have little to no impact on the associated design configuration— for example, wing shape does not influence deployment capabilities.

3.4.1 • Aircraft Type

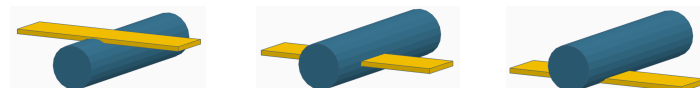


Design Consideration	Weight	Monoplane	Biplane	Lifting Body
<i>Carrying Capacity</i>	5	5	5	2
<i>Control and Stability</i>	4	4	4	2
<i>Aerodynamics</i>	3	3	2	4
<i>Manufacturability</i>	3	5	3	2
<i>Structural Strength</i>	3	3	5	3
<i>Deployment Capabilities</i>	2	3	3	3
Total		80	77	51

Figure 3.c • Figure of merit matrix for the aircraft type.

The most important design considerations this year were carrying capacity and stability. The monoplane was chosen as the most suitable aircraft type to fit these criteria, having the benefit of superb manufacturability and decent stability. A flying wing type was considered, having the best aerodynamics and velocity, but its carrying space was severely limited and would have to be scaled up heavily in order to fit the cargo needed for Missions 2 and 3. In contrast, a biplane would have very good carrying potential, as its two wings would have great wing loading. However, this comes with the tradeoff of reduced speed, increased manufacturing complexity, and higher maintenance. Plans for a biplane were eventually disregarded as the 8-foot wingspan limit allowed for sufficient lifting area to be provided by a single wing. This allowed the team to increase lift simply through the use of larger wings, which nullified the largest advantage the biplane had over the other options.

3.4.2 • Wing Placement

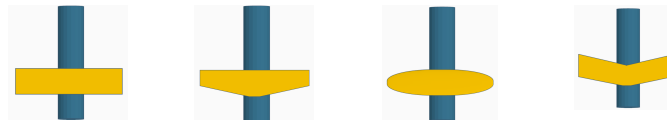


Design Consideration	Weight	High-Wing	Mid-Wing	Low-Wing
<i>Carrying Capacity</i>	5	5	2	5
<i>Control and Stability</i>	4	5	3	2
<i>Aerodynamics</i>	3	3	3	4
<i>Manufacturability</i>	3	3	2	3
<i>Structural Strength</i>	3	4	2	4
<i>Deployment Capabilities</i>	2	3	3	5
Total		81	49	76

Figure 3.d • Figure of merit matrix for the wing placement.

The choice of wing placement has the greatest impact on the stability of the aircraft. A mid-wing, one of the designs considered, would cut into the fuselage space, limiting carrying capacity. Although this problem could be solved by cutting the wing into two pieces, it would be at the expense of the structural strength, leaving them more prone to bending. Low- and high-wing configurations, conversely, could remain in a single piece without affecting payload capacity. A low-wing also benefits from a larger ground effect, reducing drag and increasing lift during Mission 3's many takeoffs and landings. Landing gear could also be attached to a low-wing configuration with less structural support than in a mid- or high-wing, leaving more space on the bottom of the aircraft for payload deployment. However, this was discarded in favor of the high wing configuration due to its improved stability characteristics. These are commonly seen on cargo airplanes as high-wings are known to be more laterally stable than middle- or low-wings due to the "keel effect," in which the center of pressure is located above the center of gravity. Furthermore, this configuration had the most clearance allowing it to more easily avoid deployed payloads or other obstacles during takeoff and landing.

3.4.3 • Wing Shape



<i>Design Consideration</i>	<i>Weight</i>	<i>Rectangular</i>	<i>Tapered</i>	<i>Elliptical</i>	<i>Swept</i>
<i>Carrying Capacity</i>	0	—	—	—	—
<i>Control and Stability</i>	4	4	5	3	2
<i>Aerodynamics</i>	3	3	4	5	4
<i>Manufacturability</i>	3	5	4	1	2
<i>Structural Strength</i>	3	4	4	3	2
<i>Deployment Capabilities</i>	0	—	—	—	—
<i>Total</i>		52	56	39	32

Figure 3.e • Figure of merit matrix for the wing shape.

Wing shape impacts the aerodynamic performance, velocity, and control of the aircraft. Rectangular wings were considered due to the ease of manufacturability which, as noted, was an important consideration due to the uncertainty of access to fabrication facilities. Elliptical and swept wings were considered unrealistic for the same reason. It was decided that a tapered wing design provided ample aerodynamic advantage without significantly increasing the complexity of fabrication. Since less lift is produced further from the wing root, decreasing chord length gradually from root to tip makes the wing more efficient while simultaneously decreasing induced drag, at the expense of needing a larger wingspan to produce the same amount of lift. Tapering the wing also reduces the strength of wing vortices at the wingtips.

3.4.4 • Empennage

Design Consideration	Weight	Conventional	T-Tail	Cruciform
Carrying Capacity	0	—	—	—
Control and Stability	4	3	5	4
Aerodynamics	3	4	4	4
Manufacturability	3	4	3	2
Structural Strength	3	5	3	4
Deployment Capabilities	2	4	5	5
Total		57	60	56

Figure 3.f • Figure of merit matrix for the empennage.

The tail plays a large role in ensuring the aerodynamic stability of the aircraft, and its design was considered accordingly. A conventional tail configuration, while simple to manufacture and structurally robust, would suffer from the turbulent airflow produced by the wings and propellers. Both a T-tail and a cruciform tail solve this problem; in the end, a T-tail was chosen for its simpler manufacturability and increased clearance, in spite of lower structural strength. T-tails are often seen paired with high-wing, multi-propeller aircraft, including cargo aircraft (although this is partially due to the presence of rear loading ramps and the necessity to avoid hot jet engine exhaust, neither of which are present in this design). The tail's vertical elevation raises it above the wing and propeller and allows it to compensate for the increased weight the plane transports when it is loaded and avoid the majority of the wake turbulence that is generated from the presence of the wings and engine. This ensures that the tail always has non-turbulent air flowing above it, which is paramount to producing the necessary lift. This is also advantageous if the plane stalls; the negative lift produced from the tail can help recover it from the dive.

3.4.5 • Propulsion System

Design Consideration	Weight	Tractor	Dual Tractor	Pusher	Tractor-Pusher
Carrying Capacity	5	3	4	3	2
Control and Stability	4	3	4	3	2
Aerodynamics	3	3	5	4	5
Manufacturability	3	4	2	2	1
Structural Strength	3	3	4	3	2
Deployment Capabilities	2	2	3	2	3
Total		61	75	58	48

Figure 3.g • Figure of merit matrix for the propulsion system.

Different propeller configurations were considered. The conventional tractor propeller is a simple yet reliable configuration. It has excellent structural loading and decent stability both on the ground and in the air. However, this option suffers from reduced lift through the creation of turbulent flow on the wing sections behind it and requires a large propeller. To fix the problem of inefficient lift, a pusher propeller was also considered since it had the best thrust and avoided the problem of turbulent flow. Unfortunately, this design also had below-average flight stability, from increased weight in the rear, and risked damage on taxiing due to the propeller rotating downwards during takeoff. The design that was chosen, the dual tractor, does not suffer from turbulent flow on the wings due to the propeller placement. This configuration is less aerodynamic than the push propeller, but it boasts superior stability in flight and great control during taxi, more so than even the single tractor propeller. The two motors allow for smaller propellers, which helps in increasing thrust. This unfortunately has the result of draining the batteries more quickly and suffers from reduced structural stability. In addition, the dual tractor configuration also creates turbulent flow on the tail, which the choice of a high tail rectifies.

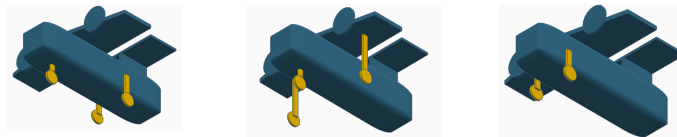
3.4.6 • Fuselage Form

<i>Design Consideration</i>	<i>Weight</i>	<i>Square</i>	<i>Rounded Square</i>	<i>Elliptical</i>	<i>Circular</i>
<i>Carrying Capacity</i>	5	5	5	3	3
<i>Control and Stability</i>	4	2	3	3	4
<i>Aerodynamics</i>	3	2	3	4	5
<i>Manufacturability</i>	3	5	3	1	2
<i>Structural Strength</i>	3	3	4	4	4
<i>Deployment Capabilities</i>	2	—	—	—	—
<i>Total</i>		63	70	54	64

Figure 3.h • Figure of merit matrix for the fuselage form.

The fuselage plays a large role in aerodynamic efficiency and payload capacity. It is also one of the largest manufacturing considerations. A square fuselage would be easiest to manufacture and its large cross-sectional area would allow for large payload capacity; however, it would create the most drag of all the designs considered. Stress concentrations would also be greater at the edges, potentially compromising structural integrity. The elliptical and circular designs provide a larger aerodynamic efficiency and present a lesser concern on stress at the edges due to the ability of the curved edges to distribute applied stress over a larger area. However, they present a much greater difficulty in manufacturing and decrease the usable cargo area due to the curved areas. The compromise between the pure square and the pure elliptical/circular designs was to round the edges of the square shape, keeping most of the storage benefits present while adding some of the aerodynamic benefits and increased stress resistance present in the elliptical/circular designs.

3.4.7 • Landing Gear



Design Consideration	Weight	Tricycle	Tip Tricycle	Tail Dragger
Carrying Capacity	0	—	—	—
Control and Stability	4	4	2	3
Aerodynamics	3	4	1	5
Manufacturability	3	4	2	5
Structural Strength	3	4	2	3
Deployment Capabilities	2	5	5	1
Total		<u>62</u>	33	53

Figure 3.i • Figure of merit matrix for the landing gear.

When choosing the landing gear, it was important to make a decision that would ensure that the plane would have the softest landing possible, the most stability in flight, and the lowest cost in performance efficiency. A static landing gear in a tricycle configuration was chosen due to the optimal stability it provided to the plane in flight and in takeoff/landing (**Figure 3.i**). Instead of running the rear landing gears across the bottom of the plane, they are instead attached to the rear fuselage in order to increase the efficiency and ease at which to accomplish unloading in Mission 3 through the bottom of the fuselage. We decided against using the taildragger landing gear due to how it would interfere with the bottom-fuselage deployment for the payload, as well as how it would obstruct the horizontal stabilizers due to the relative positioning. The location of the landing gear is chosen such that the angle between the Center of Gravity and the landing gear is approximately equal to 15 degrees. A tip tricycle was feasible before the high-wing configuration was finalized, but paired with a high-wing it would have been too structurally cumbersome.

3.4.8 • Cargo Storage and Preparation

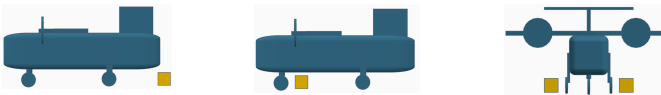


Design Consideration	Weight	Ferris Wheel	Spring-Loaded Magazine	Conveyer Belt	Motor-String System
Carrying Capacity	5	4	3	3	3
Control and Stability	4	4	2	2	2
Aerodynamics	3	2	4	4	4
Manufacturability	3	1	2	2	4
Structural Strength	3	2	3	3	3
Deployment Capabilities	2	3	3	3	3
Total		<u>57</u>	<u>56</u>	<u>56</u>	<u>62</u>

Figure 3.j • Figure of merit matrix for the cargo storage and method of preparation for deployment.

When choosing a method for the placement of cargo and the method by which the Mission 3 cargo was fed into the deployment mechanism, the team searched for a balance between carrying capacity and stability. A rotating “Ferris wheel” design was considered as an effective way to concentrate the center of gravity in a small area in order to minimize the shift in the center of gravity as boxes were deployed in Mission 3. However, its vertical height would have been too large relative to estimated fuselage sizing, and it was discarded. A spring-loaded feeding system was also considered, but it was unrealistic to find a spring that provided a reasonable amount of force across such a large range of displacements. A conveyor belt system was also proposed, but was discarded for a simpler design, a motor-string system that pulls the boxes towards the deployment mechanism.

3.4.9 • Deployment Location



<i>Design Consideration</i>	<i>Weight</i>	<i>Aft</i>	<i>Fore</i>	<i>Port/Starboard</i>
<i>Carrying Capacity</i>	0	—	—	—
<i>Control and Stability</i>	4	3	4	2
<i>Aerodynamics</i>	0	—	—	—
<i>Manufacturability</i>	3	3	3	1
<i>Structural Strength</i>	3	3	4	2
<i>Deployment Capabilities</i>	2	3	3	2
<i>Total</i>		36	43	21

Figure 3.k • Figure of merit matrix for the deployment location.

When choosing the location of the deployment mechanism, the team wanted to optimize the plane’s stability across various weight distributions in Mission 3, while ensuring that deployment would avoid triggering the shock sensors. Deployment out the side was quickly decided against; deploying the Mission 3 boxes gently enough would require too complex of a deployment system that could add an imbalanced weight to one side of the aircraft. A deployment system in the back of the aircraft, while common in many cargo planes, was decided against due to the associated shift in the center of gravity towards the back of the aircraft as more vaccine vial boxes were deployed. Guided by the old mantra, “a nose-heavy plane flies poorly, but a tail-heavy plane flies once,” the team chose to place the deployment system towards the middle of the aircraft, leading to the center of gravity shifting forwards across Mission 3. The system was placed far enough back, however, to avoid interference with the landing gear.

3.4.10 • Deployment Mechanism

Design Consideration	Weight	Aft Ramp Door	Side Door Ejection	Scissor Lift
<i>Carrying Capacity</i>	5	5	3	4
<i>Control and Stability</i>	4	2	3	4
<i>Aerodynamics</i>	0	—	—	—
<i>Manufacturability</i>	3	4	3	4
<i>Structural Strength</i>	3	2	3	3
<i>Deployment Capabilities</i>	2	3	1	5
<i>Total</i>		57	47	67

Figure 3.I • Figure of merit matrix for the deployment mechanism.

The deployment mechanism was the most heavily debated aspect of the conceptual design phase. Preliminary design had already begun before the team had procured 5G shock sensors. Two ideas were initially proposed: a simple cargo plane-style ramp door in the aft of the fuselage, and ejecting the vaccine vial boxes out the side of the fuselage through a rotating door. Both concepts were focused on deployment speed. However, once the team had secured and tested the 5G shock sensors, the side ejection idea was discarded as it was likely to trip the sensors. The scissor lift idea was produced out of an abundance of caution for the sensitive shock sensors. After the competition rules were modified so that the vaccine vial boxes used 25G sensors, it was found that the scissor lift idea was still viable due to its simplicity and small volume that allowed for additional payload in Mission 2. The scissor lift had the advantage of being able to control the descent of the boxes carefully as well as having a mechanism to eject the box from the plane. Furthermore, the scissor lift design made it easy to ensure that only one box was deployed at a time. The ramp idea was more simple, but the team had concerns over the angle of the deployed ramp. If the ramp was too shallow, the team risked the box being stuck to the ramp from friction, and if it was too steep, the box may impact the ground at unacceptably high speeds. An even greater consideration was that the ramp necessitated rearward ejection, leading to the center of gravity of the plane to shift back as the payload was deployed. Lastly, another mechanism would have been required to ensure only one box went down the ramp, thus adding to complexity and points of failure.

3.5 Final Conceptual Design

The team chose to design a monoplane with a tapered high-wing, a T-tail, a dual tractor propulsion system, rounded fuselage, a tricycle landing gear setup, and a motor-string cargo storage system that feeds into a scissor-lift deployment mechanism. An early CAD model is shown below in **Figure 3.m**.



Figure 3.m • CAD rendering of the aircraft with selected configurations.

4. Preliminary Design

This section describes the team's design methodology, the trade studies and analyses that the team performed, and the expected performance results that the analyses produced.

4.1 Overall Design Methodology

UCSD DBF determined the conceptual design of the aircraft by analyzing the scoring parameters, performing a sensitivity analysis, and identifying the optimal design configurations, as described in § 3.

The team then performed various aerodynamic and propulsion trade studies in order to determine the optimal choice of motor, propeller, wing size, and airfoil. The team also developed estimates of the aircraft's lift, drag, and stability characteristics in flight. Subteams that were responsible for performing these analyses reported to the remainder of the team with their findings, and the team worked together to address design constraints and reach satisfactory compromises. The most crucial design considerations—namely carrying capacity, stability, and manufacturability—formed the basis on which design decisions were ultimately made.

Additional analyses that focused on weight balancing and structural strength, along with input from the fabrications team, either confirmed or rejected the plausibility and effectiveness of each proposed design. Through this process, the team iterated over multiple subsystem designs, including wing and tail sizing, fuselage structure, and deployment mechanism, until it was determined that the aircraft and each composing subsystem would be capable of achieving the team's overall objective. The aerodynamics and propulsion subteams tend to drive the decisions made by the structures and fabrication subteam, but the design process is interwoven between subteams at all steps, as shown in **Figure 4.a** in a simplified manner.

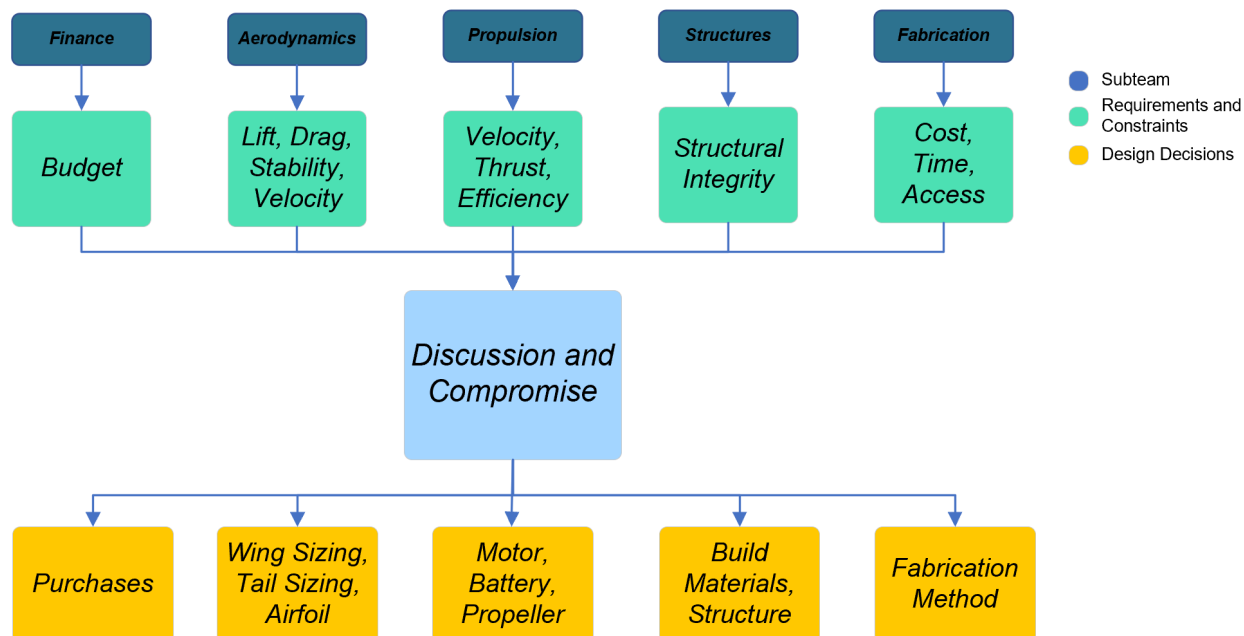


Figure 4.a • A summary of the UCSD DBF design process.

4.2 Propulsion Analysis

The team utilized an optimization script in MATLAB in order to select the best combination of batteries, motors, and propellers for the given mission airspeed requirements. The purpose of our optimization script is to choose a certain propeller and motor combination that maximizes the net efficiency of the propeller and motor combination as quantified by **Equation 4.1** while the plane endures cruising conditions. An overview of how our code works can be seen in **Figure 4.b**. For guidance in creating our code, our team referenced the multi-disciplinary design optimization (MDO) problem described by Hwang *et al.* at the University of California, San Diego [1]:

$$\eta_{net} = \eta_{prop} \times \eta_{motor} = \frac{U_x T}{VI} \quad \text{Eq 4.1}$$

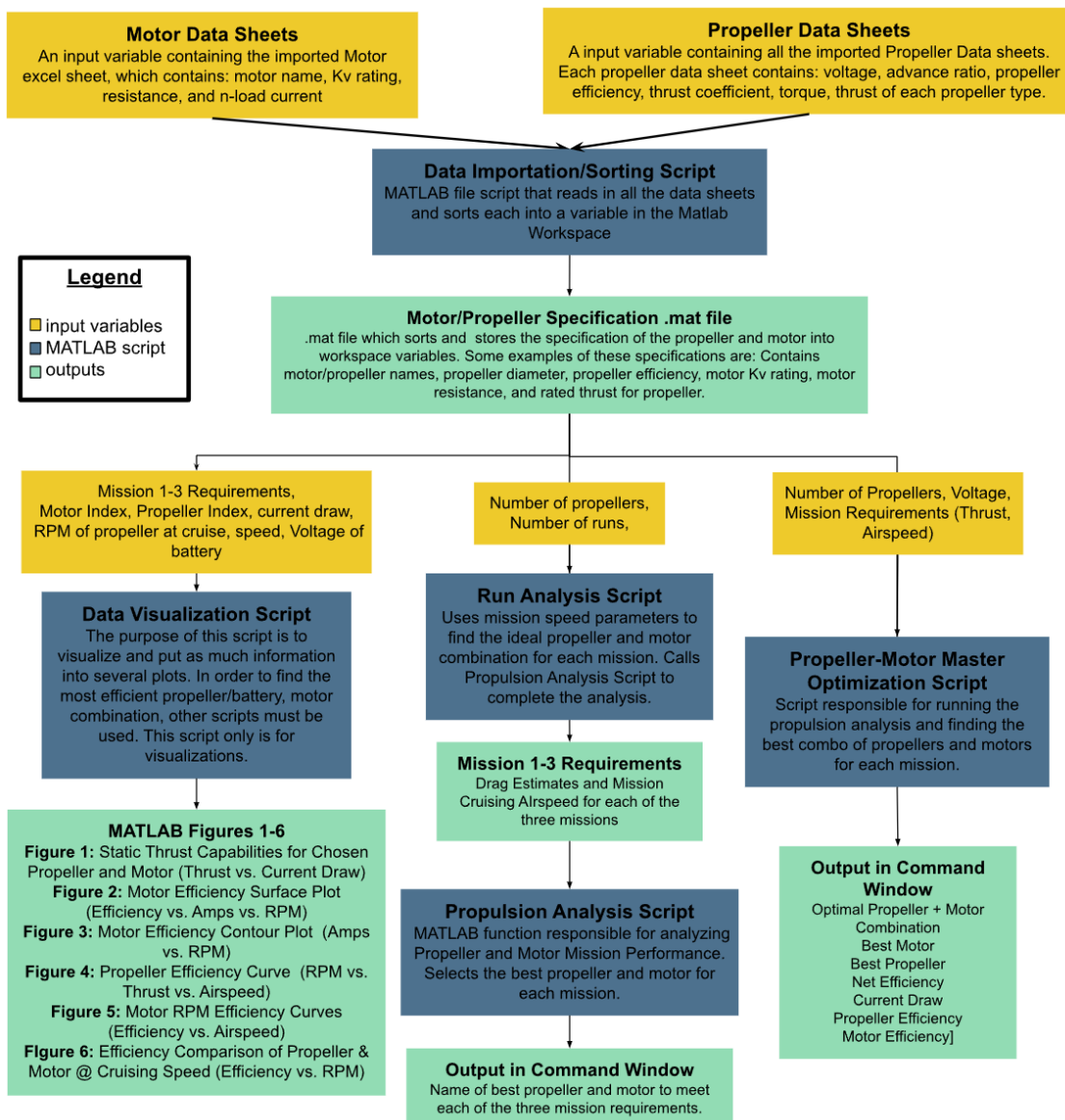


Figure 4.b • Infographic which maps inputs and outputs of each MATLAB script used by the team to pick the ideal propulsion system for the plane given certain mission parameters.

In the case of steady-level flight, assuming that airspeed and thrust are constant and neglecting voltage decay in the battery during the flight, net efficiency is optimized when current draw is minimized. Thus, a configuration that has the lowest current draw will result in a boost in the aircraft's performance and endurance during a mission.

Our code incorporates battery performance data from several hobby store websites, motor performance data from Bunge at Stanford University [2] and Scorpion documentation [3], and propeller performance data from Advanced Precision Composites (APC) [4] in order to more accurately choose which propeller and motor combinations best meets the given mission requirements. Overall, our team analyzed and iterated through about 20,000 different propulsion system combinations generated by our optimization script based on the given mission requirements. **Table 4.i** summarizes the best propulsions configuration chosen by our code based on our inputs and the data sheets used by the code.

The criteria in deciding a motor were the battery size and weight. Based on the cruise airspeed and desired thrust, our code indicated that the optimal choice was a 330Kv Scorpion SII-4025 motor. However, the battery required was an 8S battery, and due to the 100 watt-hour design constraint, this battery did not fit the desired requirements. With this consideration, we found that a 6S will fit within the fuselage and will not exceed our weight limitations. With this in mind, we evaluated that a 420 Kv Scorpion SII-4020 would be a good alternative as our main motor.

<i>Component/Parameter</i>	<i>Optimal M-1</i>	<i>Optimal M-2</i>	<i>Optimal M-3</i>
<i>Battery Specifications</i>		YOWOO 50C 6S 2200 mAh, 22.2 V, lithium-polymer	
<i>Motor Specifications</i>		Scorpion SII-4020 420 Kv	
<i>Propeller, from APC</i>		11 in. x7 in. -E	
<i>W_{prop}</i>	<i>Propulsion System Weight</i>	44.27 oz	
<i>η_{net}</i>	<i>Net Efficiency at Cruise Conditions</i>	0.5533	0.7243
			0.7243

Table 4.i • Most efficient propulsion system configuration for each mission.

To confirm that the chosen motor and battery were good options, the team performed further trade studies to visualize its performance at the expected cruise velocity, RPM, and current draw, all of which were acquired from earlier studies. Figures 4.c and 4.d provide two views of propeller performance, while Figure 4.e shows the propeller efficiency. The aircraft performs at or near maximum possible efficiency at cruise, confirming the team's choice.

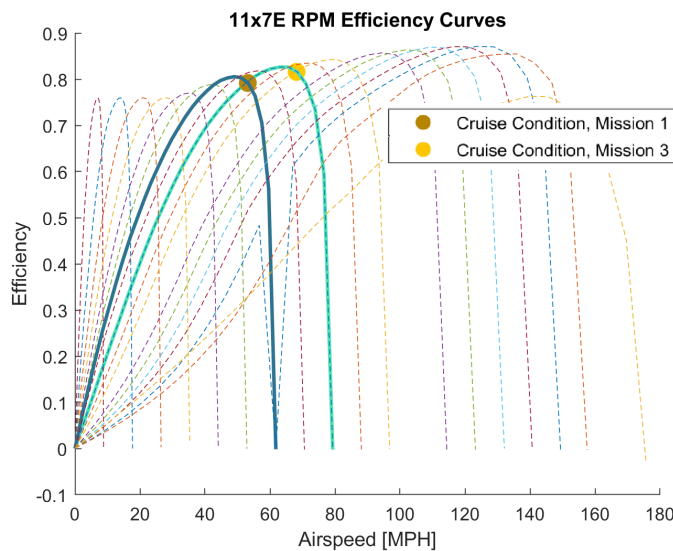


Figure 4.c • A 2D plot showing the efficiency of the chosen propeller. Each curve represents a different RPM value. The chosen configuration is shown in blue.

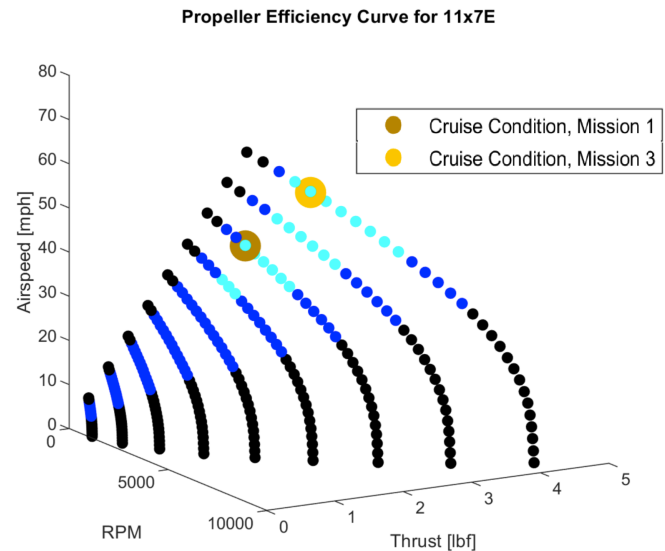


Figure 4.d • A 3D plot shown in terms of RPM, thrust, and airspeed. Colors increase in brightness as the configuration reaches ideal performance.

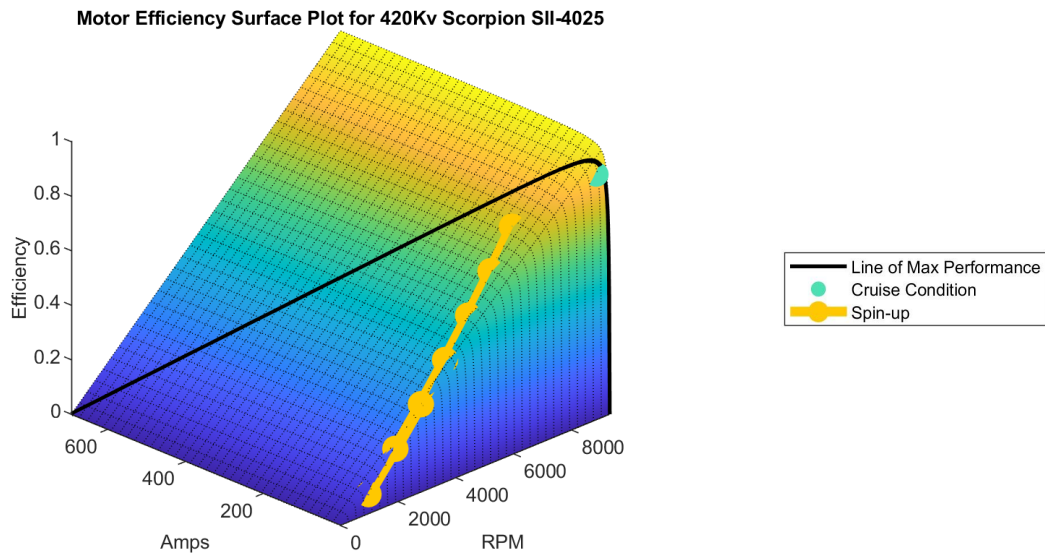


Figure 4.e • A 3D graph showing the efficiency of the chosen propeller during spin-up and cruise, relative to the line of maximum possible performance.

4.3 Fuselage Sizing

The sizing of the fuselage was designed in such a way that it can carry the deployment mechanism together with the syringes and vaccine vials (each pertaining to specific missions), and all the necessary avionics. The favorable number of the syringes, which in return determines the optimal number of the vaccine vial boxes, was chosen according to the results of a sensitivity analysis conducted by the team. Based on the results, the team designed the fuselage to carry 90 syringes and 9 vaccine vials. The configuration for Mission 2 was the main determining factor in the design of the fuselage. In that setup (detailed further in § 5) the syringes are inserted in the compartment structure in a horizontal orientation, and they run across the frame. They are stacked in four layers by alternating the top and bottom views of the syringe. Each syringe is 5.46 inches long, and the main body's diameter is 0.98 inches. The cross-sectional dimension for the fuselage was thus designed to be 8.06 inches by 6.63 inches to accommodate the length as well as the height of the stacked syringes. The sizing for the fuselage length was chosen to fit the entire deployment mechanism and to include nose and tail cones to add aerodynamic shape to the aircraft. The dimension for the entire fuselage is 48 inches.

4.4 Wing Sizing

The team incorporated a large 6.5-foot wingspan due to a variety of factors. The most important reason was the design constraint specifying a maximum linear dimension of 8 feet. This enabled the team to even consider increasing the size from last year's 5-foot wing. An increase in the wingspan would increase the aspect ratio, making the plane more aerodynamically efficient compared to last year. Next, the increased efficiency versus the structural strength had to be considered. After some discussion with the fabrication team, it was determined that since the weight of the plane would be less this year than last year, the wing won't bend and will be strong enough for an increase in the wingspan.

$$C_L = \frac{L}{\frac{1}{2} \rho V^2 S} \quad \text{Eq 4.2}$$

The team decided on the wing size by utilizing the equation for the coefficient of lift. In **Equation 4.2**, C_L is the lift coefficient, L is the lift force, ρ is the density of air, V is the velocity of the plane, and S is the wing area. By setting a limit and editing a few choice parameters, the team would be able to calculate a desirable wing size. The parameters estimated for the sizing are a maximum gross weight of 13 lbs and a velocity of 100 ft/s. The maximum limit that the team used for the wing loading, or the weight over the wing area, was 3.5 lb/ft². By utilizing **Equation 4.2**, the team found an operating lift coefficient of 0.27 that corresponds to a wing loading of 3.33 lb/ft². With the wing loading, the team found the wing area of 3.90 ft², and combined with the chosen wingspan, gave the value for the mean aerodynamic chord (MAC), 7.55 in. By rearranging **Equation 4.3** for the MAC (\bar{c}) and selecting a taper ratio (λ) of 0.4, which is common for commercial airplanes, the team was able to calculate the root chord (c_r).

$$\bar{c} = \frac{2}{3} \left(\frac{1 + \lambda + \lambda^2}{1 + \lambda} \right) c_r \quad \text{Eq 4.3}$$

With both the root chord of 10.2 in and the taper ratio, it was simple to find the tip chord to be 4 in, and thus the size of the wing was determined.

4.5 Aerodynamic Analysis

The team relied on a computational fluid dynamics (CFD) program called XFLR5 to analyze the performance of the airplane. The program provided the non-dimensional coefficients of lift, drag, and moment at various speeds. Since XFLR5 is known to underestimate drag, a component-wise drag build-up method was utilized to enhance the performance analysis.

4.5.1 • Airfoil Selection

The team began the airfoil selection process by inputting data on over a thousand airfoils, obtained from airfoiltools.com [6], into a Matlab code. Due to manufacturing constraints, the input airfoils were restricted to those with a maximum thickness that was no greater than 10% of the chord length. The Matlab code shortened the list down to a handful of airfoils with the highest glide ratios for the aircraft's expected cruise conditions. In order to obtain more accurate estimations on the performances of the remaining airfoils, the team analyzed them through the XFLR5 program. The XFLR5 analysis was done for a fixed-weight, finite-wing plane. After the analysis was performed, the team selected an airfoil with the highest glide ratio at the operating angle of attack. Based on these criteria, the airfoil choices were narrowed down to the MH60 airfoil and the Hawker Tempest airfoil, tempest3-il. The MH60 airfoil is used for flying wings and is self-stabilizing, which could interfere with our pilot's control of the plane, so it was discarded. The team decided to go with the tempest3 airfoil. As shown in **Figure 4.f**, the graph shows that the tempest3 airfoil has a glide ratio of 28 at the operating angle of attack of 2.7°.

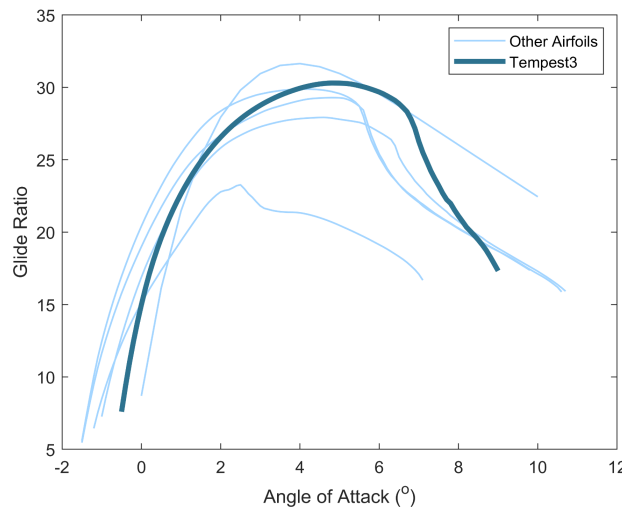
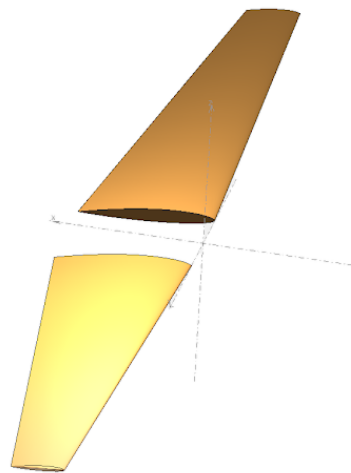
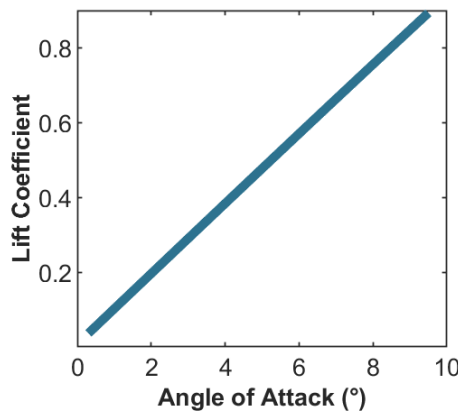
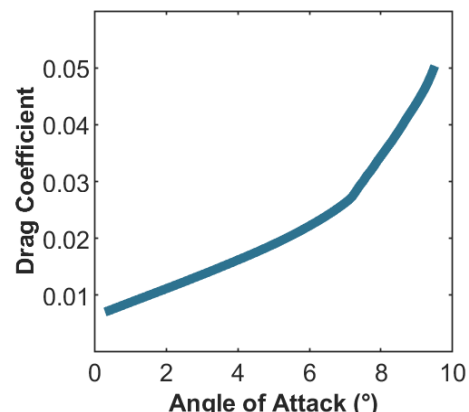
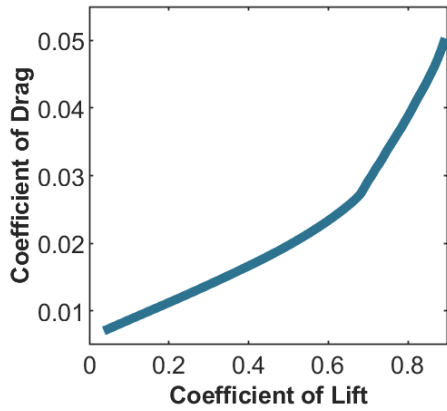
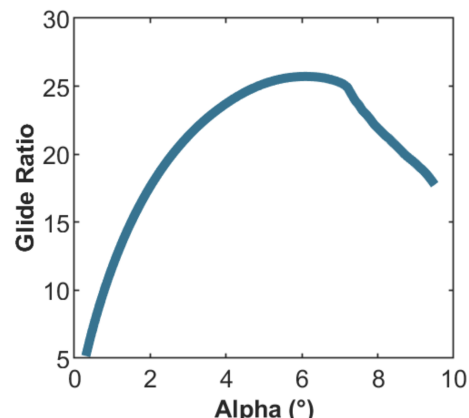


Figure 4.f • C_L/C_D vs angle of attack generated for a handful of airfoils at cruise conditions.

4.5.2 • Lift Analysis

Our team used XFLR5 to determine the aircraft's lift performance. The program performs inviscid theory analysis and viscous interpolation. XFLR5 is able to provide good interpolation and estimation of the performance of the plane with the exception of drag estimations. The team performed lift computation on only the wing, because the other parts had negligible lift. In the analysis, a gap was added between the wings to take into account the fuselage effect on lift and is displayed in **Figure 4.g**.

**Figure 4.g • Model of the wing in XFLR5****Figure 4.h • Lift coefficient vs angle of attack****Figure 4.i • Drag coefficient vs angle of attack****Figure 4.j • Drag coefficient vs lift coefficient****Figure 4.k • Glide Ratio vs angle of attack**

According to **Figure 4.h**, the maximum lift coefficient is 0.901 at an angle of attack of 9.54°. It is worth noting that the maximum lift coefficient is certainly higher than 0.901, but XFLR5 is limited in its interpolation and was unable to produce data points for higher lift coefficients and angles of attack. The optimal C_L/C_D is about 25.74 from **Figure 4.k**. The aircraft is shown to be most aerodynamically efficient at an angle of attack of 6 degrees. Based on previous years' performance data, the team knew that XFLR5 consistently underestimates drag. This led to higher C_D values and lower C_L/C_D values. This will impact the values obtained from **Figures 4.i, 4.j, and 4.k**. However, these figures still provided a rough lower-bound approximation of the drag of the plane. More accurate drag analysis is needed to estimate the plane's performance.

The XFLR5 analysis produced the stall angle and maximum lift coefficient. Using the lift coefficient equation (**Equation 4.2**), the stall velocity was calculated. The team added flaps to the wing shown in **Figure 4.6** and analyzed the lift produced with the flaps at 25° deflection. Again, using the lift coefficient equation, the velocity at takeoff was calculated. These results are displayed in **Table 4.ii**.

	Condition	Mission	Angle of attack	Lift Coefficient	Velocity
CR	Cruise Conditions	M-1	2.7°	0.27	78 ft/s
		M-2	2.7°	0.27	100 ft/s
		M-3	2.7°	0.27	100 ft/s
ST	Stall conditions	M-1	9.54°	0.901	45.7 ft/s
		M-2	9.54°	0.901	58.3 ft/s
		M-3	9.54°	0.901	58.3 ft/s
TO	Takeoff condition Flaps down at 25°	M-1	0°	0.495	61.6 ft/s
		M-2	0°	0.495	78.6 ft/s
		M-3	0°	0.495	78.6 ft/s

Table 4.ii • Angle of attack, lift coefficient, and velocity at various flight conditions

4.5.4 • Drag Analysis

Because XFLR5 tends to underestimate the component drag produced, the team instead manually computed drag using the equations derived by Professor Dieter Scholz at the Hamburg University of Applied Sciences [5]. Smaller contributions to drag—such as flap, slat, gear, and wave drag—were neglected, leaving the parasitic and induced drag produced by the main aircraft fixtures to be calculated.

The team began by computing the parasitic drag, as given by **Equation 4.4**:

$$C_{D,0} = \sum_{c=1}^n C_{f,c} \cdot FF_c \cdot Q_c \cdot \frac{S_{wet,c}}{S_{ref}} + C_{D,other} \quad \text{Eq 4.4}$$

Here, $C_{f,c}$ is the skin friction drag coefficient of the part in question, FF_c is the form factor drag coefficient of the part, Q_c is the interference factor of the part, $S_{wet,c}/S_{ref}$ is the ratio of wetted area to reference area, and $C_{D,other}$ accounts for all other drag produced by the aircraft; this is normally used for adding on drag caused by irregular parts or other phenomena, such as landing gears or pressurized air leakage from the cabin. Note that we sum for n components of the aircraft, denoted by c . Using the assumption that the flow surrounding the aircraft is turbulent, the contribution of the flow-induced shear force is as follows in **Equation 4.5**:

$$C_{f,turbulent} = \frac{0.455}{[\log(Re)]^{2.58}} \quad \text{Eq 4.5}$$

Form factor describes the drag due to pressure accumulation along the surface of a part; as such, it varies based on the aircraft component. The Mach number of the flow, the location of the thickest point of the airfoil, and the maximum thickness-to-chord length ratio are sufficient to determine the resulting form factor for the wing and empennage (**Equation 4.6**). In regards to the fuselage, the only consideration necessary to determine the form factor is the fineness ratio described in **Equation 4.7**. The Sholz document provided estimates for the flow's interference factor regarding each component and was used in the team's calculations.

$$FF_{E/W} = [1 + \frac{0.6}{x_t} \frac{t}{c} + 100(\frac{t}{c})^4] * [1.34M^{0.18}] \quad \text{Eq 4.6}$$

$$FF_F = 1 + \frac{60}{(l_f/d_f)^3} + \frac{(l_f/d_f)}{400} \quad \text{Eq 4.7}$$

From the equations, the team obtained the necessary non-dimensional values for each mission, which are summarized in **Table 4.iii**.

	Parameter	Mission	Fuselage	Wing	H. Stabilizer	V. Stabilizer	Total
C_{D_0}	Zero-Lift Drag Coefficient	M-1	0.0104733	0.01480187	0.00404648	0.00253208	0.0317140
		M-2	0.0100336	0.0140940	0.00384498	0.00240782	0.0302468
		M-3	0.0100336	0.0140940	0.00384498	0.00240782	0.0302468
C_F	Turbulent Skin-Friction Drag Coefficient	M-1	0.00373352	0.00527970	0.00588135	0.00565635	-
		M-2	0.00357675	0.00502720	0.00558848	0.00537877	-
		M-3	0.00357675	0.00502720	0.00558848	0.00537877	-
$FF_{F/E/W}$	Form Factor	-	1.090047964	1.16814443	1.100625	1.100625	-
Q_c	Interference Factor	-	1	1.2	1.03	1.03	-

Table 4.iii • Non-dimensional drag parameters for each component.

Continuing, the magnitude of induced drag— or the resultant drag created by the presence of lift— is known to be quadratically proportional to the lift coefficient; it also is inversely related to the aircraft wing's aspect ratio and the Oswald efficiency factor (**Equation 4.8**). The document by Sholz suggests that the Oswald efficiency factor relies on the total number of engines and the wing's aspect ratio, taper ratio, and thickness-to-chord length ratio (**Equation 4.9**).

$$C_{D,i} = \frac{C_L^2}{\pi e AR} \quad \text{Eq 4.8}$$

$$e = \frac{1}{(1 + 0,12 M^6)[1 + 0.142 + f(\lambda)AR(\frac{10t}{c})^{0.33} + \frac{0.1(3N_e + 1)}{(4 + AR)^{0.8}}]} \quad \text{Eq 4.9}$$

The induced and total drag coefficient values for each configuration are documented below in **Table 4.iv**.

Parameter	M-1	M-2	M-3
e	0.828	0.828	0.828
C_{D0}	0.0317	0.0302	0.0302
C_{DI}	0.0031	0.0031	0.0031
C_D	0.0348	0.0333	0.0333

Table 4.iv • Efficiency factor and drag coefficients for each mission.

4.6 Stability and Control Analysis

The plane's stability is heavily dependent on the tail. In order to determine the size of the tail, the team used **Equation 4.10** for the horizontal tail volume ratio:

$$C_H = \frac{S_H \cdot l_H}{S_W \cdot MAC} \quad \text{Eq 4.10}$$

In this equation, C_H is the horizontal tail volume ratio or coefficient, S_H is the horizontal tail area, l_H is the distance of the tail's aerodynamic center to the airplane's center of gravity, S_W is the wing area, and MAC is the mean aerodynamic chord of the wing. For the tail volume horizontal ratio, we expect to get a value between 0.5 to 1. Our tail volume ratio is on the higher end, this year, at 1.04; however, this tail size allows us to control the stability of the plane well according to the analysis.

Using XFLR5, the team analyzed the static margin and pitching moment of the aircraft. The neutral point was found to be 7.758 in from the leading edge of the root chord of the wing. The team then defined the desired center of gravity for each mission and calculated the expected static margin. The neutral point is the hard limit for how far back the center of gravity can be pushed in the plane while maintaining stability. The team selected the center of gravity to be at the quarter-chord of the wing to ensure structural integrity of the plane. If the center of gravity is at the quarter-chord, it will also be at the aerodynamic center of the wing, the location along the wing in which the moment is constant regardless of the angle of attack. With the center of gravity and the neutral point, the static margin can be calculated using **Equation 4.11**.

$$SM = \frac{NP - CG}{MAC} \quad \text{Eq 4.11}$$

From the equation, SM is the static margin, NP is the neutral point, CG is the center of gravity, and MAC is the mean aerodynamic chord of the wing. The static margin is a measure of how statically stable the plane will be. Generally, commercial airplanes have static margins between 10% and 20%. The static margin for all missions this year is 67.1%. Although this isn't within the range, previous years have static margins in the percentages of 50s and 60s, so this is no cause for concern. The neutral point of an aircraft is very difficult to calculate, and since we simplify the analysis to only the wing and tail of the plane, there is bound to be some discrepancy in the location of the neutral point.

Another stability condition is given by the moment coefficient curve, which must be negative and intercept the x-axis at the operating angle of attack. This condition is satisfied (**Figure 4.I**). From the graph, it is revealed that from a range of 2 inches to 3 inches for the position of the center of gravity, there is a range of 2.3° to 2.8° for the angle of attack. The gold horizontal line represents the center of gravity pushed to the neutral point and supports the definition of the neutral point having a constant moment for differing angles of attack. **Figure 4.m** shows the variation in the lift coefficient for the changes in the center of gravity. The expected range for the lift coefficient is between 0.23 and 0.27. The analyses are reassuring, but test flights must still be performed to accurately trim the tail and stabilize the plane during flight.

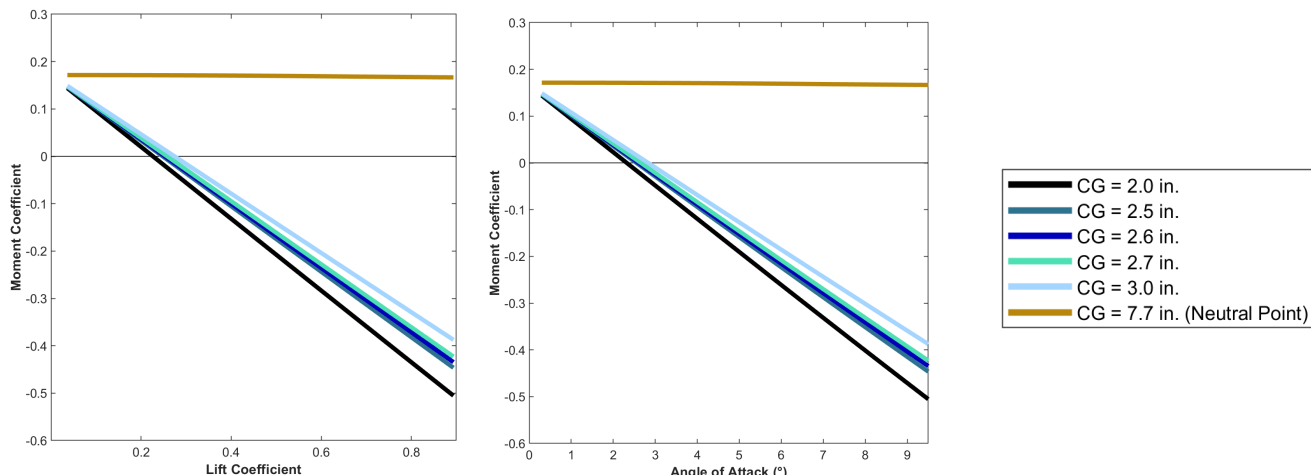


Figure 4.I • Moment coefficient vs. lift coefficient for various locations of the center of gravity.

Figure 4.m • Moment coefficient vs. angle of attack for various locations of the center of gravity.

4.7 Mission Model

DBF UCSD built upon MATLAB code and analyses from previous years in order to develop a mission model that provided a more accurate estimate of the aircraft's performance at the chosen and estimated parameters for each mission.

Based on user inputs of mass, maximum load factor, lift coefficient, wing surface area, etc., the team's flight simulation code first determines the velocity the aircraft will fly during the 1000 ft. long straights and the banked-angle turn portions of the course. From the combined velocity estimates, the code calculates the estimated flight time in which the aircraft will complete a single lap. A high-level overview of the code can be found in **Figure 4.n** below. The code allowed the team to develop estimates of the aircraft's performance, which are summarized in **Table 4.v**.

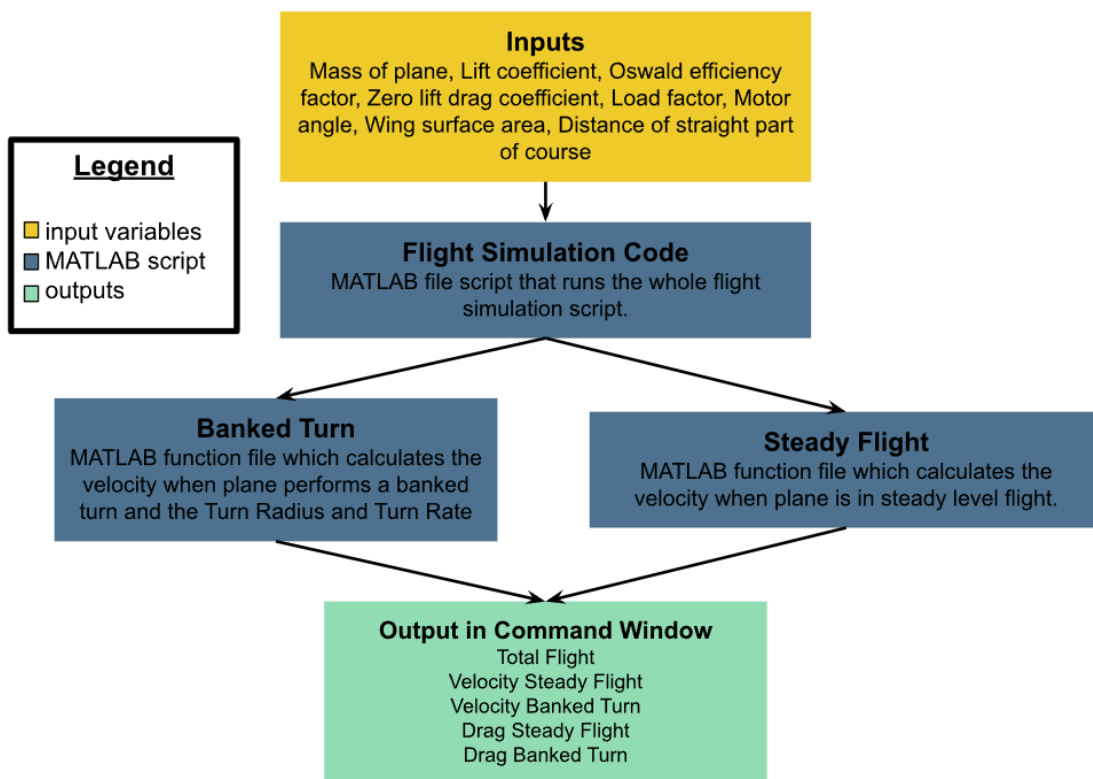


Figure 4.n • Infographic which maps all of the inputs and outputs for the MATLAB scripts which simulate the aircraft performance while flying in the course.

<i>Parameter</i>	M-1	M-2	M-3
W_G	Takeoff weight 8.0 lb	13.0 lb	13.0 lb
V_{TO}	Takeoff velocity 61.6 ft/s	78.6 ft/s	78.6 ft/s
I_{CR}	Cruise power draw 25.4 A	22.2 A	22.2 A
T_{TF}	Endurance 10.4 min.	12.0 min.	12.0 min.
V_{SL}	Steady-level speed 82.0 ft/s	102.9 ft/s	102.9 ft/s
D_{SL}	Steady-level drag 0.9 lb	1.4 lb	1.4 lb
V_{BT}	Banked-turn speed 93.4 ft/s	117.3 ft/s	117.3 ft/s
D_{BT}	Banked-turn drag 1.2 lb	1.8 lb	1.8 lb
	Lap time 25.9 s	21.3 s	21.3 s
E_L	Per-lap energy draw 182.7 mAh	131.4 mAh	131.4 mAh

Table 4.v • Model-generated estimated flight performance parameters.

Uncertainty from the model is due mainly to simplifying assumptions within the code. These include the assumptions that airspeed and thrust are constant and that no voltage decay occurs in the battery during the flight. Wind, pressure variation, and other complex external forces are neglected. Since the code was developed before the aircraft was constructed, it also draws upon assumptions and data collected in previous years that determined, among other things, maximum wing loading and climb angle. Finally, the model is unable to account for mid-flight pilot error that may result in a suboptimal flight path or turning rate. The values in **Table 4.v** served as optimistic initial estimates to be verified or updated as additional testing data was obtained.

5. Detail Design

In the detail phase of the design process, UCSD DBF finalized design decisions. They analyzed the structural capabilities and flight performance of their aircraft and determined the architecture of the sensor, its deployment mechanism, and other subsystems.

5.1 Final Design Parameters

Tables 5.i and **5.ii** summarize the aircraft's finalized dimensions, design characteristics, and electrical specifications.

	Dimension	Fuselage	Wing	Horizontal stabilizer	Vertical stabilizer	Total
<i>b</i> or <i>L</i>	Span or length	48.75 in	6 ft	26 in	14 in	55 in
<i>H</i>	Height	7.27 in	—	—	—	22.5 in
<i>W</i>	Width	6.375 in	—	—	—	78 in
<i>C</i> _{root}	Root chord	—	10.2 in	6 in	7.5 in	—
<i>C</i> _{tip}	Tip chord	—	4 in	6 in	6 in	—
MAC	Mean aerodynamic chord	—	7.55 in	6 in	6.75 in	—
<i>S</i>	Reference area	—	562.3 in ²	312 in ²	94.5 in ²	—
<i>b</i> ² / <i>S</i>	Aspect ratio	—	10.08	2.17	2.07	—
Airfoil	Hawker Tempest (tempest3)					

Table 5.i • The aircraft's final dimensional characteristics. Values listed as applicable.

Tail servomotors	KST X08H	ESC	Frsky Neuron
Stall torque	73.6 oz.-in. at 8.4 V	Current rating	80.0 A
Servomotor speed	0.09 sec/60° at 8.4 V	Battery	YOWOO 50C 6S
Servomotor weight	0.335 oz.	Number of cells	6
Wing servomotors	KST X10 Mini	Pack voltage	22.2 V
Stall torque	104.2 oz.-in. at 8.4 V	Pack weight	11.28 oz
Servomotor speed	0.09 sec/60° at 8.4 V	Motor	Scorpion SII-4020
Servomotor weight	0.811 oz.	Kv rating	420 Kv

Table 5.ii • Electrical and mechanical specifications of the aircraft.

5.2 Structural characteristics

During flight and upon landing, the aircraft experiences different loads resulting from the wing and tail lift, thrust from the motors, and reaction forces on the landing gears. **Figure 5.a** shows a free body diagram of these forces. The DBF team analyzed the loads in the processes of making structural design choices of the aircraft, which are explained in detail in the following section.

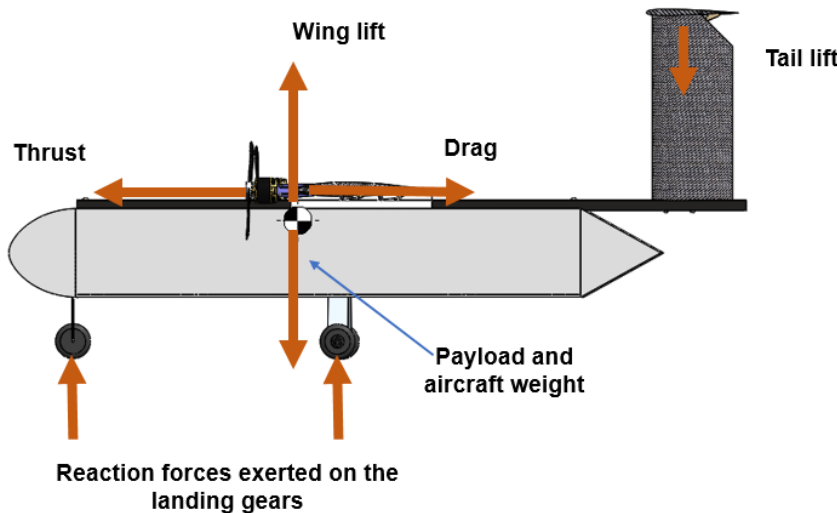


Figure 5.a • Free body diagram of the aircraft

In addition to the external forces experienced on the aircraft, the team also conducted analysis on the aerodynamic limits in which the plane can safely operate. The results determine that the aircraft can withstand a maximum of 2.5 positive load factor, and a minimum load factor of -1.5. The stall, cruise, and dive speeds for all three missions are obtained from **Table 4.iv** in § 4.3.2. The V-n diagram together with a vertical gust envelope are shown in **Figure 5.b** and **Figure 5.c**. Since M2 and M3 have similar speed requirements, they are both represented in **Figure 5.c**.

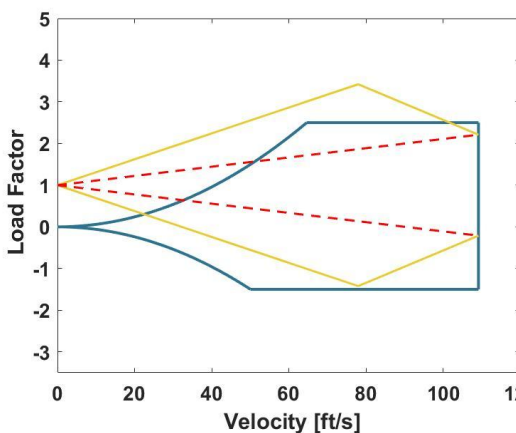


Figure 5.b • V-n diagram for Mission 1

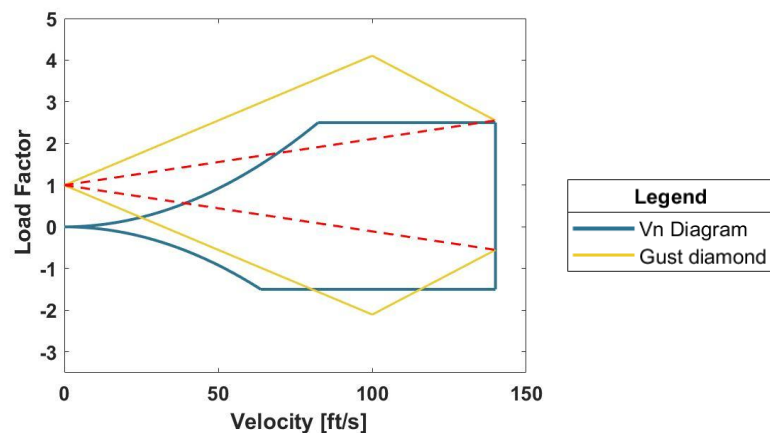


Figure 5.c • V-n diagram for Missions 2 and 3.

5.3 System and subsystem architecture

The team designed the aircraft to best meet the mission requirements by investigating individual subsystems and their integration into the complete aircraft.

5.3.1 • Fuselage

The aircraft fuselage was designed to incorporate payload carrying capacity into its structure to minimize volume. The team decided to employ a monocoque 1/8 in. balsa wood and plywood structure that is primarily constructed using glue, thereby minimizing complexity and weight. Due to time constraints, two-dimensional components were emphasized to allow for quick laser cutting and rapid prototyping. The wood frame fits in a bounding box that is 37.75 in. lengthwise, 6 in. widthwise, and 6.25 in. heightwise. The top and bottom plates are manufactured out of continuous sheets with lightening holes to increase rigidity. The lightening hole pattern on the top plate minimizes weight while the bottom plate has slots to ensure that the vaccine vial boxes do not get stuck on a corner. Vertical columns placed along the length of the plane connect the top and bottom plates to transfer landing forces and provide torsional stability. A carbon fiber 0.75 in. X 0.83 in. boom that is fastened to the top of the structure via M5 screws and inset T-nuts distributes vertical forces. 3/16 in. foam board is used as an aerodynamic nose and skin. Where the foam board is attached permanently, it is epoxied to the wood fuselage framing. Removable side panels, avionics hatch, and rear hatch are connected to a simple hinge and secured by velcro and tape.

The payload compartment is capable of holding up to 90 syringes (**Figure 5.f**) and 9 vaccine vial boxes (**Figure 5.g**). A foam skin with removable side panels and a rear hatch allow access to load payloads. A cutout on the bottom plate allows the scissor lift mechanism to sit flush with the exterior and minimize aerodynamic drag. Details of the payload compartment are displayed in **Figures 5.d** and **5.e**.

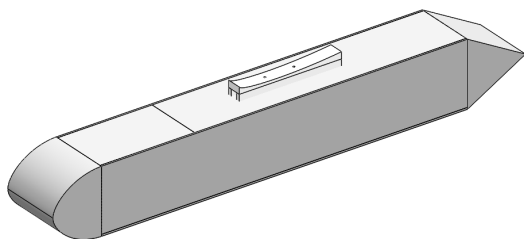


Figure 5.d • The fuselage of the aircraft.

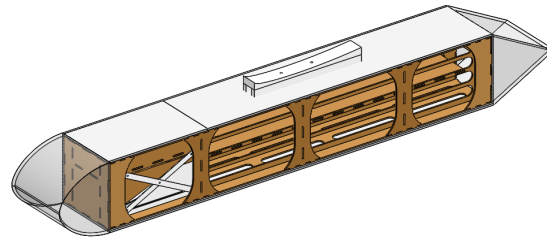


Figure 5.e • The interior structure of the fuselage, consisting of the compartment and the deployment mechanism.

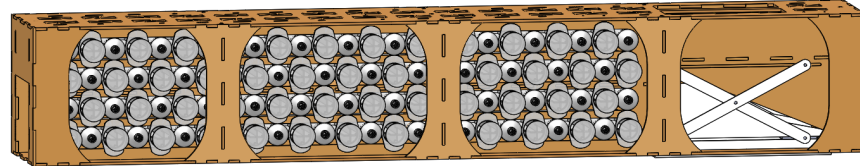


Figure 5.f • Payload compartment that's capable of holding 90 syringes for M2.

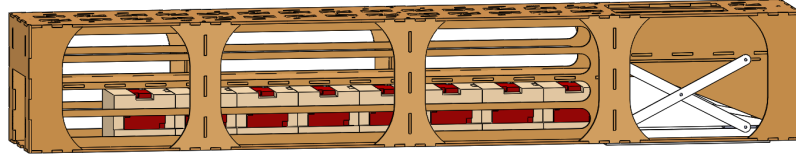


Figure 5.g • Payload compartment with the capacity of holding 9 vaccine boxes for M3.

5.3.2 • Wing

The wing has a 0.4 taper ratio, and a wingspan of 6.5 ft. It is made of foam and reinforced with carbon fiber. A high wing configuration was chosen to increase stability and ground clearance. The increased height allows for larger propellers for the wing-mounted motors and eliminates the possibility of obstruction of the vaccine package on the ground. The wing is mounted via a 3D printed flush mount and two M5 bolts that run through the wing to the fuselage. **Figure 5.h** shows the wing configuration.

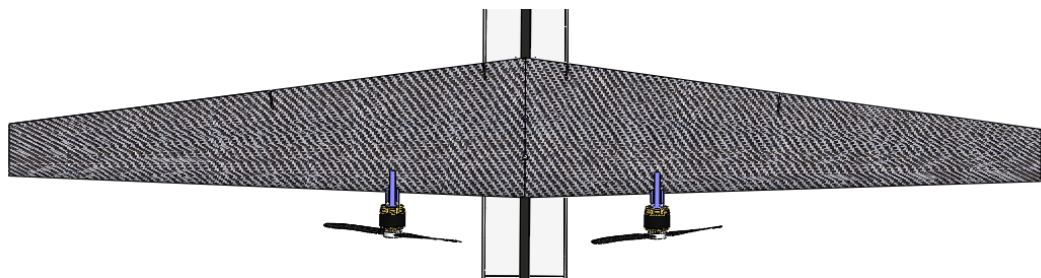


Figure 5.h • Tapered wing of the aircraft.

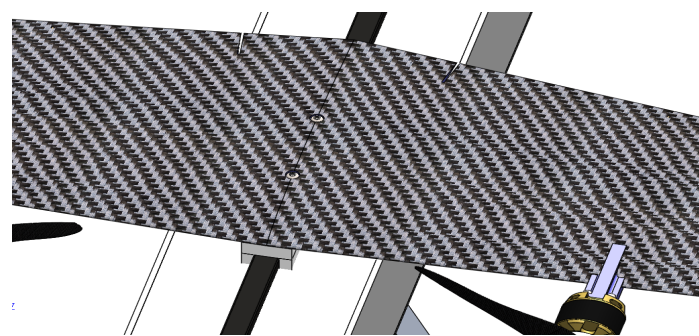


Figure 5.i • Wing fastened to the carbon fiber boom using two screws.

5.3.3 • Empennage

The tail section has a rectangular horizontal stabilizer that is 26 in. x 6 in. dimensions, and a 14 in. high vertical stabilizer. They are manufactured using high-density foam, and overlaid with carbon fiber for structural integrity. With a high wing configuration, the team opted for a T-tail arrangement for the empennage, so that the turbulent flow generated by the propulsion system and the wings does not affect the airflow over the horizontal stabilizer. This configuration requires a strong vertical stabilizer, and therefore the team chose to embed threaded metal rods that pass through the carbon fiber boom located in the fuselage's tail, and fastened using hex nuts (**Figure 5.i**). The metal rods enable the tail to withstand high pressure forces during flight, as well as allow for a strong connection to the fuselage. The empennage is shown in **Figure 5.j** and **5.k**.

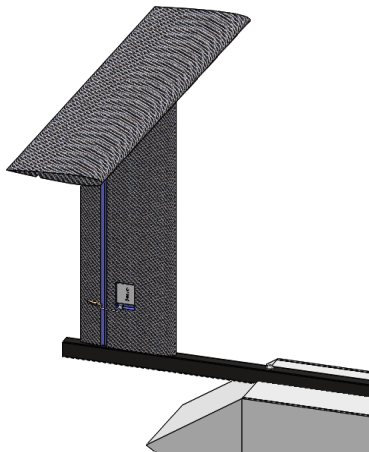


Figure 5.j • The tail section of the aircraft.

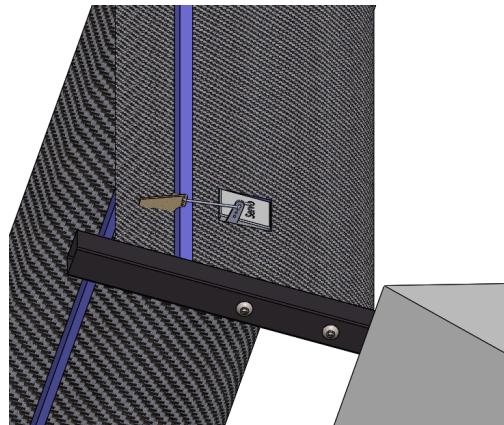


Figure 5.k • Empennage fasteners.

5.3.4 Landing Gear

The tricycle landing gear is an easy configuration for smooth landing and take-off. It is also an optimal design consistent with a high wing aircraft. The main landing gear runs across the bottom of the fuselage, mounted near a set of vertical columns, and measures 6 in. long with a 4 in. clearance above the ground (**Figure 5.l**). The height dimensions are chosen in order to allow the scissor lift enough space to deploy each vaccine vial package. It also gives ample space between the propeller blade and the ground.

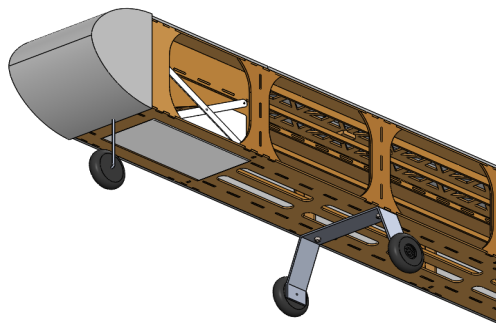


Figure 5.l • Display of the nose and main landing gears.

A finite element analysis using Von Mises simulation in Abaqus was conducted to determine the maximum load and displacement of the main landing gear. The analysis took into account a 1.5 Safety Factor when considering the load exerted on the landing gear. The results of the analysis are shown in **Figure 5.n.i** and in **Figure 5.n.ii** with dimensions in units psi and inches, respectively. The yield strength was 2.1×10^4 psi. The analysis shows that the landing gear can support 3 times the weight of the aircraft.

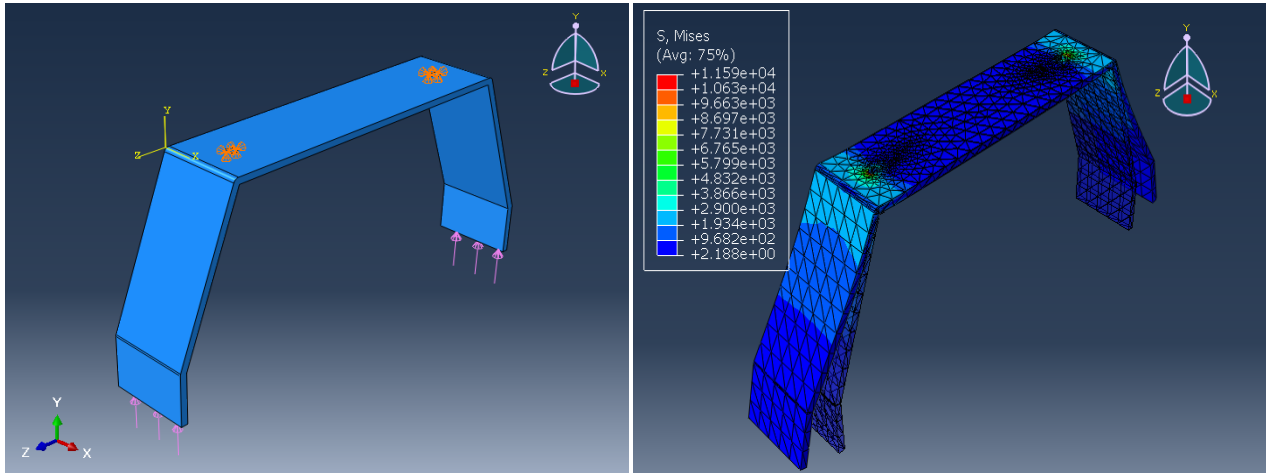


Figure 5.m Representation of the point of application of the forces exerted on the landing gear.

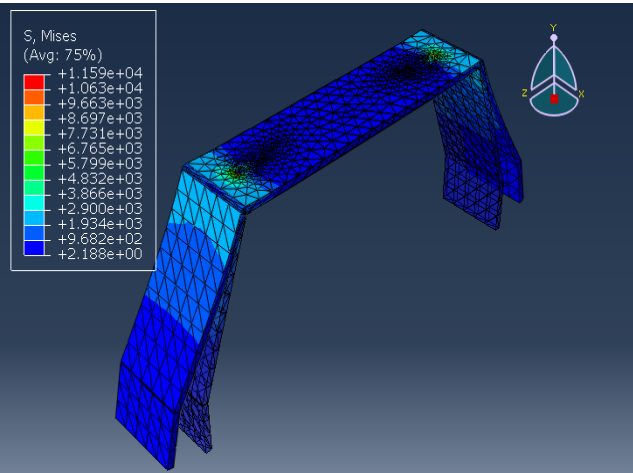
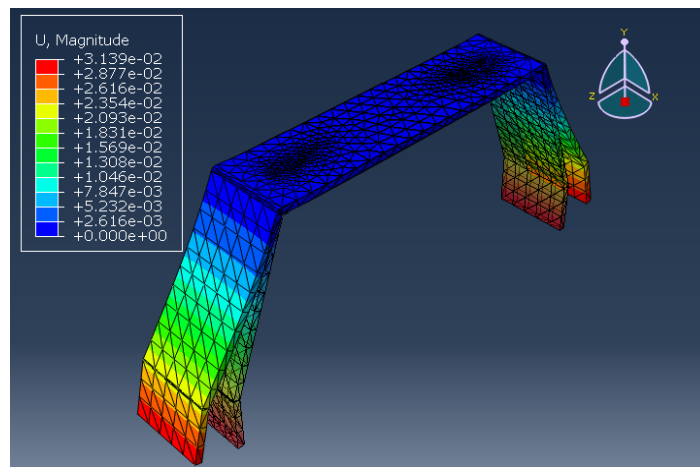


Figure 5.n Stresses in pounds per square inch experienced by the main landing gear.



. **Figure 5.o** Displacement experienced at different locations of the landing gear during landings.

5.3.5 • Motor Mount

The team elected to 3D print a motor mount that sits flush with the profile of the leading edge of the wing (**Figure 5.p**). It was found that 100% infill and attachment via epoxy produced sufficient strength to support the motors. The carbon fiber skin on the wing was sanded to produce a rough surface to increase adhesion strength. The mounts were designed to be wide enough to withstand the tensile and torsional forces.

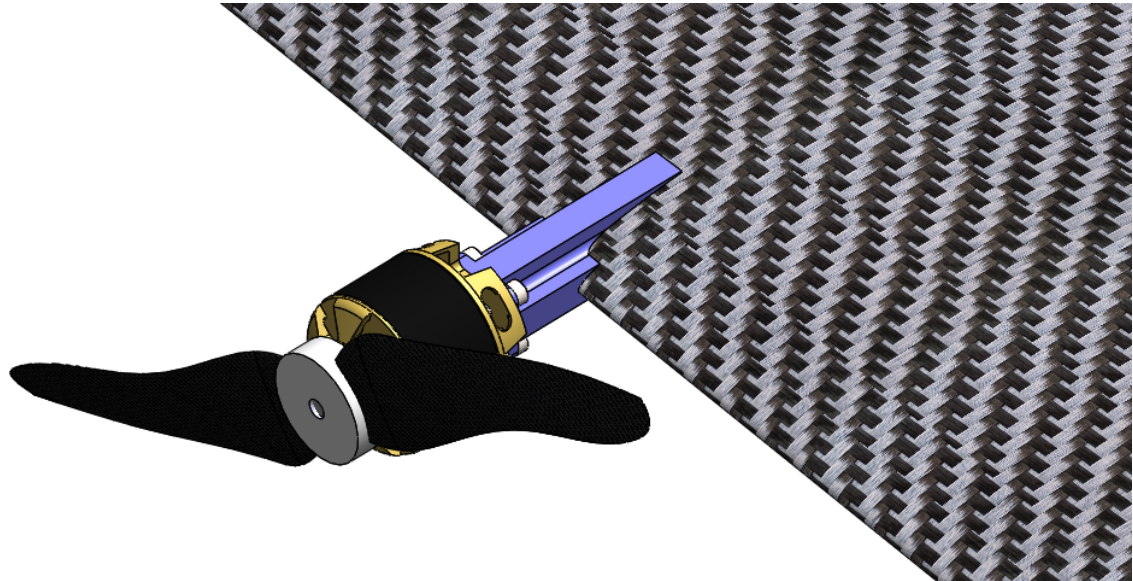


Figure 5.p • Motor mount with the motor and propeller attached to it.

5.3.6 • Deployment Mechanism

Figures 5.q and 5.r depict the deployment mechanism as a scissor lift with 3D printed components. It is placed towards the nose of the aircraft for two primary reasons: 1. The center of gravity of the payload shifts forward, ensuring that the aircraft will remain stable. 2. The packages are ejected aft of the lift body, thus allowing the plane to taxi forward. The design incorporates one set of scissors to maximize rigidity and to increase the length of travel of the bottom guide bar that doubles as a pusher mechanism to eject the box from the lift. The lift holds the box with the largest face (3.5 in. x 3.0 in.) resting downwards to minimize the height that the box may tip and impact the ground, and it descends 3.5 in. before the box is fully ejected, allowing a 1 in. clearance between the top face of the box at the point of complete ejection and the bottom of the fuselage. The lift is controlled via a fuselage-mounted 6 in. linear actuator that connects to the top guide bar. A NEMA 8 motor mounted to the fuselage winds a string that pulls the boxes forward into the elevator.

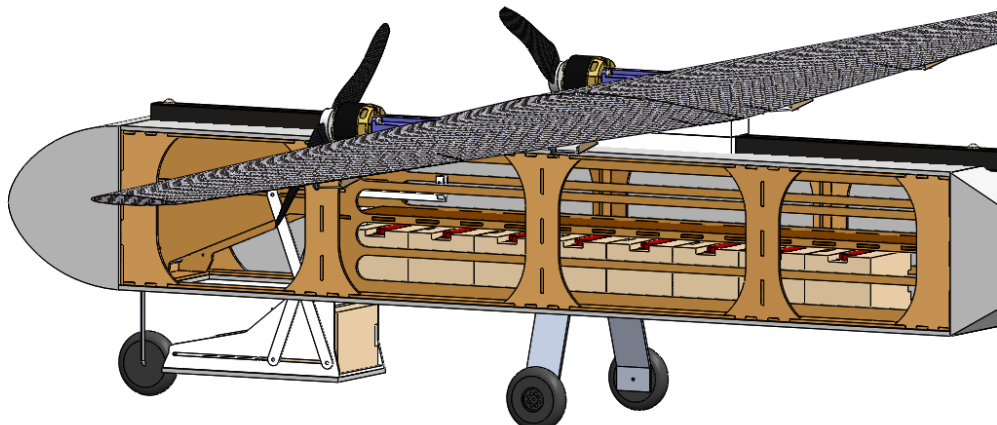


Figure 5.q • The scissor lift deployment mechanism.

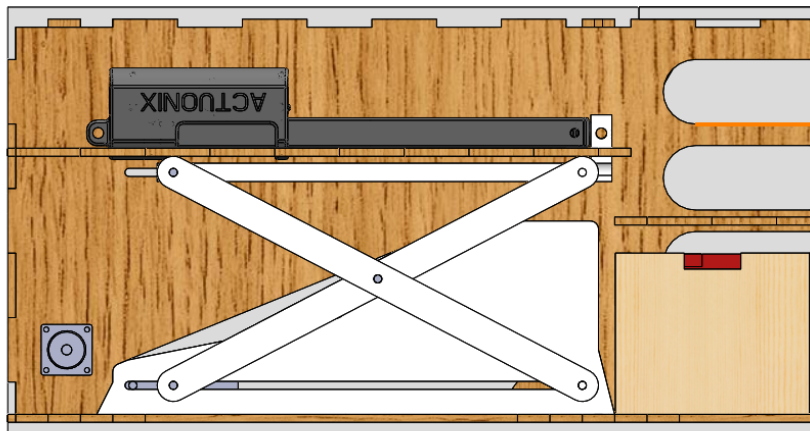


Figure 5.r • Scissor lift close-up.

5.3.7 • Avionics

Given the mission's parameters of delivering vaccination components, the team focused mostly on the design of the fuselage in order to carry the necessary payloads. The fuselage was built to carry vaccine syringes and vaccine vial packages. A special mechanical device was designed to deploy and deliver the vaccine vial packages in a manner that would allow for one vaccine vial package to be deployed per lap. The fuselage was also designed to be able to carry 10 syringes in a fashion that keeps the syringes stable throughout the entire flight in order to complete 3 laps before coming to a safe landing. To drive the motors, the team chose 32-bit FrSky Neuron 80 ESCs for its ability to measure current, ESC temperature, motor speed, power consumption, and voltage; fast throttle response; and smooth motor cogging. They also daisy-chained a FrSky pitot-tube into the S.Port to record the aircraft's speed. The team chose KST X08N as tail V5 servo motors and X10-710 as wing servo motors because of their wide voltage ranges and compact aluminum construction. At 8.4 V, the X08N produces 39 oz.-in. of torque; the X10-710 produces 104.16 oz.-in. of torque. Their avionic system runs on a higher voltage (8.4 V). This reduces the possibility that the carbon fiber wing's construction causes a receiver brownout, improves its connection strength, and increases the servo motors' torque output. **Figure 5.s** shows the avionics configuration.

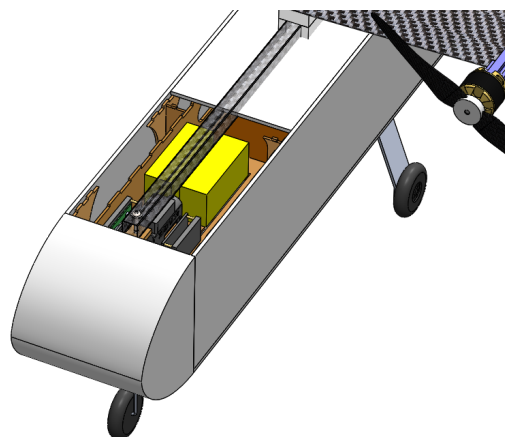


Figure 5.s • Battery, transmitters, and receiver are placed in the front part of the fuselage.

5.4 Weight and balance

Table 5.iii includes the plane's component weights and positions from the motor firewalls toward the aircraft's rear (**+X**-direction) and below the thrust line (**+Z**-direction), along with the resultant weight and center of gravity positions for all configurations. Since the aircraft is symmetrical about the centerline, the distance along the **Y**-direction can be ignored.

Component and count		Case	Weight	X-distance	Z-distance
Battery	x2	M-1	1.4 lb.	-9.2272 in.	-2.8821 in.
		M-2	1.4 lb.	-8.1872 in.	-2.8821 in.
		M-3	1.4 lb.	-8.5972 in.	-2.8821 in.
Empennage	x1	ALL	0.5 lb.	30.4683 in.	10.409 in.
ESC	x2	ALL	0.25 lb.	-13.7887 in.	-3.5156 in.
Fuselage	x1	ALL	1.32 lb.	4.0903 in.	-4.6651 in.
Landing gear	x1	ALL	0.63 lb.	0.3623 in.	-10.5382 in.
Motor	x2	ALL	1.27 lb.	-0.9185 in.	0 in.
Receiver	x1	ALL	0.03 lb.	-12.8096 in.	-2.2165 in.
Wing	x1	ALL	1.5 lb.	4.8924 in.	0.0662 in.
Deployment mechanism	x1	ALL	0.62 lb.	-11.305 in.	-6.9491 in.
Syringes	x90	M-2	3.92 lb.	8.023 in.	-4.92 in.
Vaccine Vial Boxes	x9	M-3	4.5 lb.	4.6313 in.	-6.6594 in.
Total		M-1	7.52 lb.	1.197 in.	-2.0204 in.
		M-2	11.44 lb.	-3.108 in.	-2.915 in.
		M-3	12.02 lb.	-2.226 in.	-3.489 in.

Table 5.iii • Weight and balance. Distances in the X-direction are measured from the motor mounts; distances in the Z-direction are measured from the thrust line.

5.5 Expected performance

The analyses performed in § 4 allowed the team to develop expectations for the aircraft's flight during cruise and banked flight. The team also implemented a new flight simulation in order to more accurately predict the aircraft's performance throughout the entire flight. The model, written in MATLAB, utilizes user-inputted data obtained from the earlier flight simulation code and other trade studies in order to describe the initial conditions of the aircraft and flight location. Then, using a detailed aerodynamic model and a fourth-order Runge-Kutta method to approximate changes in state, it simulates a full course lap. The code outputs a matrix containing relevant state variables including lift, drag, and velocity over the course of the flight. It also produces a map of the aircraft's flight path (**Figure 5.u**). **Figure 5.t** provides an overview of the code.

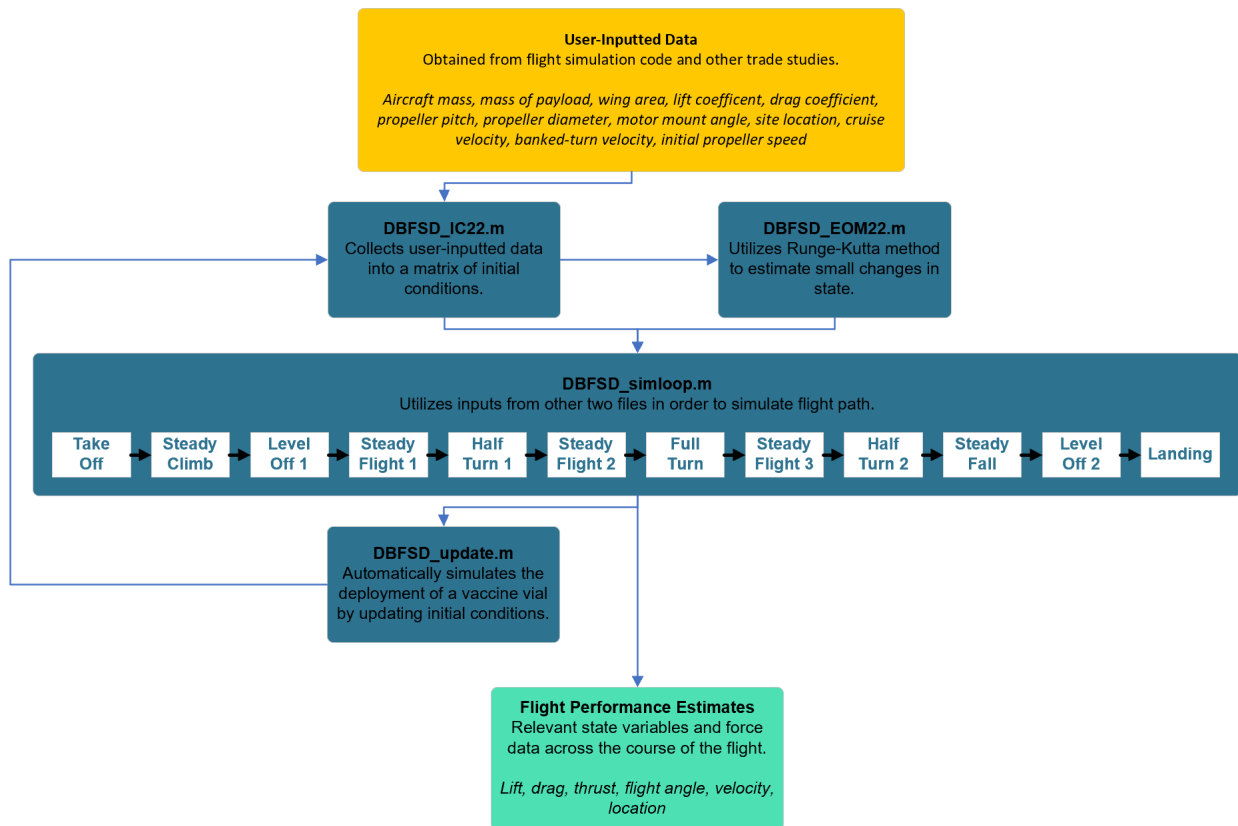


Figure 5.t • A flowchart describing the components of the code used to estimate mission performance.

A simulation of Mission 3 was developed in order to better understand how variations in weight would impact the flight path and performance of the aircraft. Some variations are shown in **Figure 5.v**; each flight path varies in weight by $\frac{1}{2}$ pound, approximately the weight of the vaccine vial boxes.

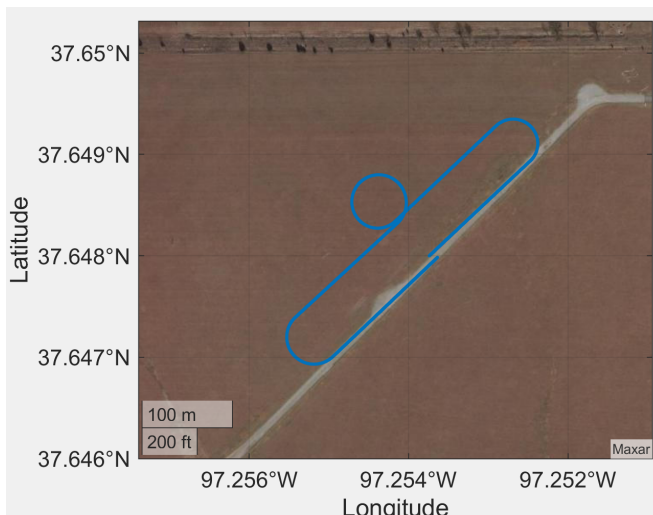


Table 5.u • The simulated flight path overlaid on satellite imagery of the competition location in Wichita, Kansas.

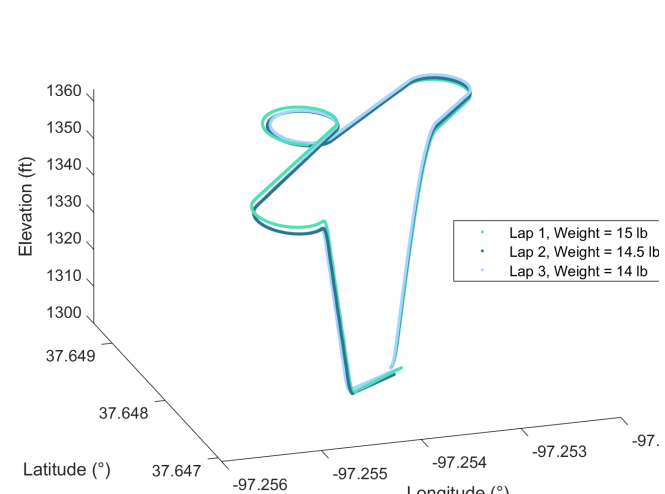


Figure 5.v • A 3D plot of the flight path with varying aircraft weights.

The expected flight performance metrics are summarized in **Table 5.iv**. This table is similar to **Table 4.v**, but values have been added and updated as necessary. **Table 5.v** summarizes the expected mission performance of the aircraft. Values are derived from the MATLAB code as well as the sensitivity analysis, which factors in score distributions from previous years, along with a confident estimate of the team's relative performance, to generate a rough projected mission score.

Parameter	M-1	M-2	M-3	
W_G	Takeoff weight	7.5 lb	11.4 lb	12.0 lb
x_{TOG}	Takeoff distance	14.9 ft	18.4 ft	18.9 ft
v_{TO}	Takeoff velocity	59.7 ft/s	73.6 ft/s	75.5 ft/s
I_{CR}	Cruise power draw	12.7 A	11.1 A	11.1 A
T_{TF}	Endurance	10.4 min.	12.0 min.	12.0 min.
v_{SL}	Steady-level speed	79.6 ft/s	98.4 ft/s	101.1 ft/s
D_{SL}	Steady-level drag	1.2 lb	1.59 lb	1.62 lb
v_{BT}	Banked-turn speed	93.4 ft/s	114.3 ft/s	117.3 ft/s
D_{BT}	Banked-turn drag	1.3 lb	1.71 lb	1.72 lb
	Per-lap energy draw	133.6 mAh	194.6 mAh	196.6 mAh

Table 5.iv • Model-generated estimated flight performance parameters.

Parameter	M-1	M-2	M-3	
T	Lap time	35.7 s	31.9 s	33.7 s
x_{TOG}	Total Flight Time	112.4 s	105 s	303.3 s
nL	Number of laps	3	3	9
Sc	Projected mission score	1 of 1	1.9 of 2	2.8 of 3

Table 5.v • Model-generated estimated mission performance parameters.

5.6 • Drawing package

The following pages contain the drawing package for UCSD DBF's 2021-22 fly-off aircraft.

6. Manufacturing Plan

The following section evaluates several manufacturing methods and materials to build the aircraft. It also describes the chosen assembly methods and outlines the team's manufacturing timeline.

6.1 Investigation of manufacturing processes

To find a production method that meets the design criteria of a high-performance and reliable aircraft and suits their current manufacturing capabilities, UCSD DBF investigated multiple methods of production (**Table 6.i**).

Methods	Advantages	Disadvantages
3D-printing	<ul style="list-style-type: none"> - Low cost - Capable of making very complex parts - Parts can be quickly printed 	<ul style="list-style-type: none"> - Relatively fragile - Parts size restricted to printer size - Parts are isotropic
Balsa wood	<ul style="list-style-type: none"> - Low cost - Parts can be made expediently 	<ul style="list-style-type: none"> - Requires complex digital modeling to design
Carbon fiber composites	<ul style="list-style-type: none"> - High stiffness to weight ratio - Lightweight 	<ul style="list-style-type: none"> - Expensive - Time-consuming layup process - Blocks certain frequencies of radio signals
Fiberglass composites	<ul style="list-style-type: none"> - Does not block radio frequencies - High strength to weight ratio 	<ul style="list-style-type: none"> - Comparatively weaker than carbon fiber - Shrinks and distorts when wetted with epoxy resin - Soaks up more resin increasing weight
Foam-core structures	<ul style="list-style-type: none"> - Can act as spacers to increase overall strength - Allows for quick prototyping 	<ul style="list-style-type: none"> - Requires sanding for smooth surface
Hollow molded structures	<ul style="list-style-type: none"> - Close resemblance to design profiles - Can be created using various materials 	<ul style="list-style-type: none"> - Time-consuming to fabricate the mold

Table 6.i • Production methods in consideration.

6.2 Assembly method selection

After assessing the production methods listed in **Table 6.i**, the team optimized for assembly methods of specific components for the aircraft.

6.2.1 • Fuselage

The fuselage inner frame was chosen to be constructed out of $\frac{1}{8}$ inch balsa wood and plywood sheets (**Figure 6.a**). Composites were ruled out for the fuselage because of the need for complex molds, labor, and time. The inexpensive balsa wood sheets were cut using a laser cutter and different components were joined together using box joints. Box joints increased the surface area between the wood and the glue to obtain a stronger bond. Once the fuselage structure with the package deployment mechanism was manufactured, removable panels of paper-coated foam were added to the wood frame to make the fuselage more aerodynamic.



Figure 6.a • Two views of the fuselage balsa wood inner frame.

6.2.2 • Wing

The team used a hot-wire cutting CNC to cut the shape of the airfoil out of foam for manufacturing the wing (**Figure 6.b**). Using a hand router, channels were cut into the foam core and servo cables were laid inside to avoid running wires over the finished wing. Another channel was cut and a carbon fiber spar was placed between the two halves of the foam cores for added rigidity. Carbon fiber sheets were then placed on nonstick mylar sheets and saturated with epoxy resin. For weight reduction, any excess resin was blotted with paper towels. To create durable joints for control surfaces, kevlar strips were placed underneath the carbon fiber which would be later cut to make moveable flaps and ailerons. The control surfaces were then covered with gap sealing tape for added aerodynamic efficiency. For structural integrity, extra carbon fiber was also added to the leading edge of the wing. Then the foam core was inserted between the carbon fiber-covered mylar sheets and vacuum bagged.

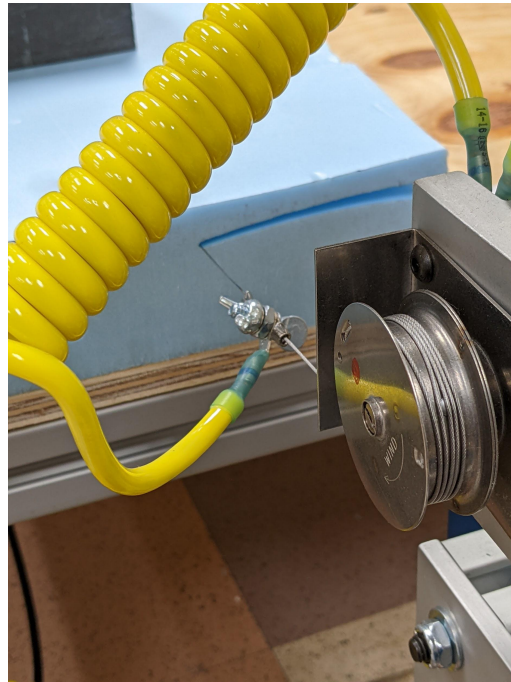


Figure 6.b • The hot-wire cutter in the process of cutting out the foam wing.

6.2.3 • Tail

The tail was constructed in a similar process as the wing. Carbon fiber was overlaid over a foam core cut using a hot wire. In order to securely mount to the structural carbon fiber boom, the T-shaped tail section has two all-threaded rods inserted into it which were then fastened with nuts. Two 3-D printed L brackets were glued to the vertical and horizontal stabilizers to strengthen the joining of the two, and thin kevlar strings were tied at both ends of the vertical stabilizer to the fastened rods on the fuselage for tensioning and keeping the empennage intact. All control surfaces were covered with gap-covering tape and servos were covered with aerodynamic shrouds.

6.2.4 • Landing Gear

The landing gear was custom manufactured out of 1.5 inch wide and 1/8 inch thick aluminum bar stock. The bar was cut to length and two M5 holes were drilled that correspond to holes in the floor of the wood fuselage framing. It was then bent by 110 degrees on either side to form the legs. The tips of the legs were further bent to be vertical and holes were drilled to allow for the installation of wheels.

6.3 Manufacturing timeline

In light of the COVID-19 pandemic, subsequent public health restrictions restricted the team's access to their workshop. Their prototype design could not be fabricated; thus, they could only fabricate one aircraft for the 2021-22 contest season. The sole prototype constructed during this competition season served both as a testing and competition plane. **Figure 6.c** shows the current manufacturing timeline.

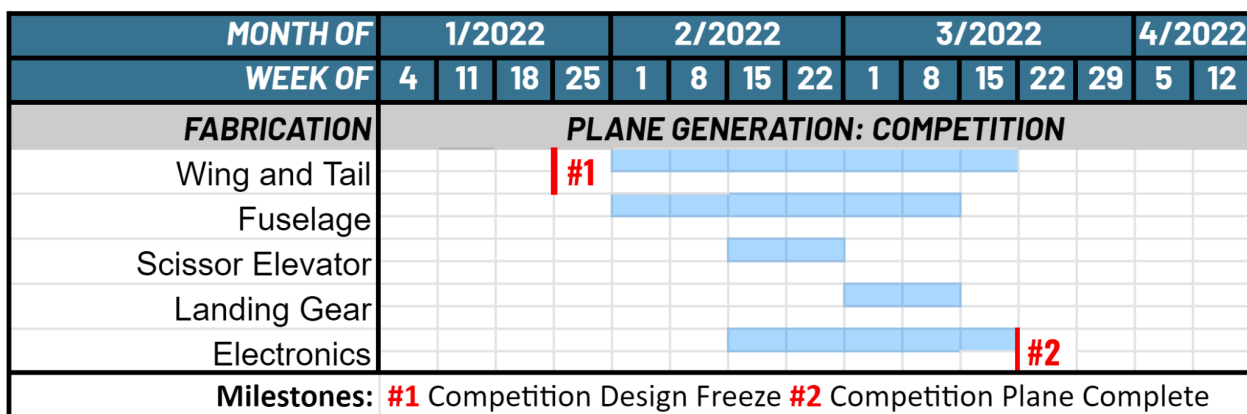


Figure 6.c • A Gantt chart displaying the planned fabrication schedule.

7. Testing Plan

To gather flight data and optimize the performance of its competition aircraft, UCSD DBF created a plan to test the aircraft's subsystems. This section discusses the team's comprehensive testing process.

7.1 Testing Schedule

The team has planned two test flights and various other subsystem tests throughout the 2021-22 competition season; the test schedule is shown in **Figure 7.a**. With the limited techniques and tools available to us, the team is in the process of conducting several tests on the aircraft's propulsion set-up, structural components, and other subsystems.

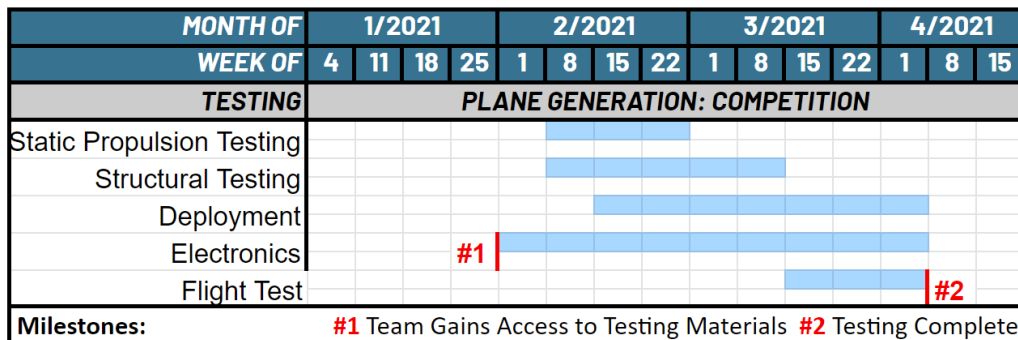


Figure 7.a • A Gantt chart displaying the planned testing schedule.

7.2 Ground Testing

To minimize the risk of harm to the flight team and aircraft, extensive ground testing will be performed prior to the first flight test. The completed, ongoing, and planned tests are documented below.

7.2.1 • Static propulsion testing

To verify that it performed similarly to their theoretical calculations, the team used an RC Benchmark dynamometer to measure the current, motor speed, static thrust, and voltage of the selected propulsion system across various throttle settings (**Figure 7.b**). This data was collected and used to verify that the motor, battery, and propeller configuration was working properly and would be capable of providing the necessary level of thrust across the entire flight.



Figure 7.b • A mid-test photo of the static propulsion test stand, motor, battery, and propeller.

7.2.2 • Structural testing

The team has planned several tests before flight to validate the structural integrity of the aircraft. So far, the team has tested the carbon fiber spar's ability to support the aircraft's full weight (**Figure 7.c**). When the aircraft is fully assembled, the team will perform bending and torsion tests on the wings, as well as place weights on the wing roots to simulate the maximum loading conditions from earlier calculations. The team will conduct two wingtip tests—while the aircraft is unloaded and fully loaded—to test the safety of its fuselage and wing joints. The team will also perform drop testing on the fuselage and landing gear to ensure that it maintains integrity in case of a heavy-impact landing.



Figure 7.c • One of the loading tests performed on the carbon spar to ensure its integrity.

7.2.3 • Payload securement testing

To ensure that the payload does not adversely move and affect the aircraft mid-flight, the loaded aircraft was manually manipulated to simulate mid-flight pitch, roll, and yaw maneuvers. These tests ensured that the Mission 2 syringes did not come loose and that the Mission 3 shock sensors did not trigger. The shock sensors were also experimented on heavily in order to gain an intuitive sense of the limits to which they could be subjected before triggering. The team will also perform timed simulations of Ground Mission payload loading in order to measure and improve our speed, develop more efficient methods of loading, and ultimately maximize our competition score.



Figure 7.d • A photo of the fuselage frame being loaded with the Mission 2 payload and the 3D-printed deployment mechanism being cleared of support material.

7.2.4 • Deployment mechanism testing

To ensure the reliable deployment of vaccine vial boxes for Mission 3, the deployment mechanism will be tested extensively to ensure stability and consistency. The mechanism will first be tested in the DBF fabrication room to ensure that all nine vaccine vial boxes can be deployed without error. It will also be tested prior to each test flight to confirm that it performs satisfactorily on the rugged runway terrain. The pilot will also practice taxiing towards and away from a designated drop-off area to ensure that the deployed box does not impede the aircraft's movement.

7.3 Flight Testing Plan

Progressive tests utilizing the deployment mechanism and increasing amount of payloads will be performed until we reach the experimental maximum for our desired performance.

7.3.1 • Risk Reduction and Preflight Checklist

Given that the team only plans to manufacture a single aircraft, reducing the risk of a mid-flight failure or crash is of the utmost importance. Before flying the aircraft, the team and the pilot will be required to verify the conditions specified in **Figure 7.e** and receive signatures from the attending lead members and advisor.

Preflight Checklist			
Propulsion		Controls	
Propeller Direction?	<input type="checkbox"/>	Receiver Connection?	<input type="checkbox"/>
Propeller Secured?	<input type="checkbox"/>	Control Surfaces Responsive?	<input type="checkbox"/>
Wiring Secured?	<input type="checkbox"/>	Telemetry Software On?	<input type="checkbox"/>
Motor Mounted Properly?	<input type="checkbox"/>	Visual Inspection?	<input type="checkbox"/>
Batteries Charged?	<input type="checkbox"/>	Aircraft	
Battery Voltages +/- 3V?	<input type="checkbox"/>	CG Verified?	<input type="checkbox"/>
Receiver Pack Charged?	<input type="checkbox"/>	Wing bolts tight?	<input type="checkbox"/>
Receiver On?	<input type="checkbox"/>	Hatches Closed?	<input type="checkbox"/>
Connection Secured?	<input type="checkbox"/>	Landing Gear Tight?	<input type="checkbox"/>
Payload		Signatures	
Weight Verified?	<input type="checkbox"/>	Pilot	_____
Payload Secure?	<input type="checkbox"/>	Faculty Advisor	_____
Scissor Lift Working?	<input type="checkbox"/>	Project Manager	_____
Shock Sensors Reset?	<input type="checkbox"/>	Date	_____

Figure 7.e • List of safety checks performed prior to each test flight.

7.3.2 • Flight Testing Schedule

The team plans to perform 9 test flights over the course of 4 weeks (**Table 7.i**). The first flights, to be performed on 12 March 2022, will first test the propulsion system performance, structural integrity, and overall flight capabilities of the aircraft with no payload. This strategy will allow the team to find and fix unforeseen problems before performing further tests.

Subsequent tests will include a gradually increasing payload weight with no deployment attempted. These gradual shifts in weight will allow the pilot to handle the aircraft more effectively. The final flights will be performed on 2 April. The first flight will simulate Mission 2 with a fully-loaded set of syringes. The final two flights will be full simulations of Mission 3 performed with a full payload and all necessary landings, deployments, and takeoffs.

Date and location	Flight number	Simulated mission	Payload weight
19 March 2022 San Diego, California	1	M-1	0.0 lb.
	2	M-1	0.0 lb.
	3	M-3	1.0 lb.
	4	M-3	2.0 lb.
	5	M-3	3.0 lb.
	6	M-3	4.5 lb.
2 April 2022 San Diego, California	7	M-2	4.5 lb.
	8	M-3	4.5 lb.
	9	M-3	4.5 lb.

Table 7.i • List of test flights.

During test flights, the team will collect telemetry data detailing current draw and cruise speed. The team will also manually measure takeoff distance, lap time, and flight endurance. These values will serve as a final confirmation of the team's design choices and reveal the necessity for any final design adjustments, such as a decrease in payload or shifts in weight and balancing. The data will be cross-referenced with the values obtained in trade studies and analyses in order to understand why the divergences occurred and to improve the analyses' accuracy for future years. The team will also consult with the pilot, a UCSD DBF alumnus with many years of R/C piloting experience, to implement changes that will improve the handling or performance of the aircraft.

8. Performance Results

The following section documents the results of the tests described in § 7.

8.1 Aircraft and Subsystem Performance

Results of the tests that the team has performed thus far are compiled below.

8.1.1 • Propulsion Testing

Table 8.a shows the power, thrust, and voltage measured when the chosen propulsion configuration was operated at the current draw values estimated from the propulsion analysis.

Mission	Current	Power	Thrust	Voltage
M1	12.7 A	284.5 W	1.62 ft./s.	22.4 V
M2, M3	11.1 A	251.8 W	1.43 ft./s.	22.6 V

Table 8.a • Static motor test results.

The tests revealed that the expected current draw for Missions 2 and 3 is likely an underestimation; the motor will likely need to draw more current in-flight in order to produce the necessary amount of thrust. However, the propulsion system will be operating at a higher advance ratio in flight than on the static test stand, meaning that the original values could still be accurate; more data will need to be collected from flight tests in order to make a definitive judgment.

The team also encountered several easily remedied issues, including a faulty ESC and unbalanced propellers creating excess vibrations at certain throttle ranges. Overall, though, the Scorpion motors are a good solution for the team's performance goals. They provided enough thrust and operated efficiently during the static tests. The LiPo packs supplied enough current and did not overheat. The tests so far have confirmed the team's propulsion choices.

8.1.2 • Structural Testing

The balsa wood fuselage frame was found to be an excellent lightweight option and supported the full Mission 2 payload. The syringes rest more-or-less securely in the fuselage slots, but additional work will need to be done to develop more efficient methods of loading and determine whether other methods of securing the syringes to each other will be worth the additional weight. Additionally, the carbon spar was capable of supporting the equivalent weight of the fully-loaded aircraft. The scissor lift body printed without error, fit snugly into the fuselage frame, and was found to be sturdy enough for the team's needs. The 3D-printed scissor lift arms, however, did not provide the necessary level of rigidity, and the team opted to replace them with laser-cut polycarbonate.

8.2 Flight Performance

As described in § 3.2, UCSD DBF was unable to access fabrication materials and facilities from the beginning of November 2021 until the end of January 2022 due to COVID-19 policies and other circumstances outside of the team's control. The team worked diligently throughout February, but ultimately decided to delay the flight tests until March, after the report is due, rather than risk the integrity of the aircraft and the safety of the club members with a rushed fabrication process. As a result, flight performance data is not yet available.

8.3 Future work and concluding remarks

In this report, UCSD DBF documented our past, current, and future work to design, analyze, manufacture, and fly an aircraft at this year's Design/Build/Fly competition. The team recognizes that a large amount of work remains before the aircraft is competition-ready. As we have in the previous four weeks, the team plans to dedicate all possible effort in the coming weeks towards completing the fabrication and assembly of the aircraft, as outlined by our updated timeline. The remainder of the necessary ground and flight testing will then be performed. The team plans to be completely competition-ready following the conclusion of the second test flight, but has allocated the additional three weeks before the competition to perform any final design adjustments or replacements.

In spite of administrative and pandemic-related obstacles, UCSD DBF is confident that we will bring an aircraft to this year's Design/Build/Fly competition that is capable of successfully competing and achieving the objectives established in § 1.

9. Bibliography

- [1] Hwang, J. T., Arnav V. J., and Tae H. H., ["Large-scale multidisciplinary design optimization—review and recommendations."](#) AIAA, San Diego, CA, June 2019.
- [2] Bunge, R., ["Motor/propeller performance analysis and estimation."](#) Stanford University, 8 April 2016.
- [3] ["Motors."](#) Scorpion.
- [4] ["Performance data."](#) Advanced Precision Composites.
- [5] Scholz, D., ["Drag Prediction,"](#) *Aircraft Design - an Open Educational Resource (OER) for Hamburg Open Online University (HOOU)*.
- [6] "Airfoil database search," retrieved 3 November 2021. <http://www.airfoiltools.com/>